

## Supplementary Information for

### Transformable Helical Self-Assembly for Cancerous Golgi Apparatus Disruption

*Rong Sheng Li,<sup>†, ‡, ||</sup> Jiahui Liu,<sup>†, ||</sup> Hu Shi,<sup>§, \*</sup> Ping Ping Hu,<sup>#</sup> Yao Wang<sup>†</sup>, Peng Fei Gao<sup>†</sup>, Jian Wang<sup>†</sup>, Moye Jia<sup>⊥</sup>, Hongwei Li<sup>⊥</sup>, Yuan Fang Li<sup>Φ</sup>, Chengde Mao<sup>†, T, \*</sup>, Na Li<sup>‡\*</sup>, Cheng Zhi Huang<sup>†, \*</sup>*

<sup>†</sup>Key Laboratory of Luminescence Analysis and Molecular Sensing (Southwest University), Ministry of Education, College of Pharmaceutical Sciences, Southwest University, Chongqing 400715, P. R. China.

<sup>‡</sup>Beijing National Laboratory for Molecular Sciences (BNLMS), Key Laboratory of Bioorganic Chemistry and Molecular Engineering of Ministry of Education, Institute of Analytical Chemistry, College of Chemistry and Molecular Engineering, Peking University, Beijing 100871, P. R. China.

<sup>§</sup>School of Chemistry and Chemical Engineering, & Institute of Molecular Science, Shanxi University, Taiyuan 030006, P. R. China.

<sup>#</sup>Chongqing Key Laboratory of Natural Product Synthesis and Drug Research, School of Pharmaceutical Sciences, Chongqing University, Chongqing 401331, P. R. China.

<sup>⊥</sup>Beijing Nuclear Magnetic Resonance Center, College of Chemistry and Molecular Engineering, Peking University, Beijing 100871, P. R. China

<sup>Φ</sup>Key Laboratory of Luminescence and Real-Time Analytical System, Chongqing Science and Technology Bureau, College of Pharmaceutical Sciences, College of Chemistry and Chemical Engineering, Southwest University, Chongqing 400715, P. R. China.

<sup>T</sup>Department of Chemistry, Purdue University, West Lafayette, IN, 47907 USA.

<sup>||</sup>R.S.L. and J.L. contributed equally to this work.

## Contents

1. Instruments and materials .....	S5
2. Peptide self-assembly in aqueous medium .....	S5
3. Multilamellar vesicle (MLV) preparation .....	S6
4. TEM study of L-HFs self-assembly of F <sub>4</sub> KY in the Golgi and MLV .....	S6
5. Quantification of cytokines.....	S6
6. <i>In vivo</i> imaging and treatment study.....	S7
7. Cell viability test and fluorescence imaging.....	S7
8. Flow cytometry.....	S7
9. Sample preparation for MALDI-TOF-MS.....	S8
10. NMR methods.....	S8
11. Simulation methods for F <sub>4</sub> KY self-assembly .....	S8
12. Simulation methods for the interaction between L-HFs self-assembly and membrane .....	S8
13. Statistical analysis .....	S9
14. Chemical structure of C <sub>6</sub> RVRRF <sub>4</sub> KY .....	S10
<b>Figure S1</b> Chemical structure of three different functional units of C <sub>6</sub> RVRRF <sub>4</sub> KY.....	S10
15. Morphology and mechanism of L-HFs self-assembly of F <sub>4</sub> KY .....	S11
15.1 Self-assembly of F <sub>4</sub> KY .....	S11
<b>Figure S2</b> Extinction spectra of F <sub>4</sub> KY before and after self-assembly. ....	S11
<b>Figure S3</b> Representative AFM images of left-handed helical fibrils (L-HFs) self-assembly of F <sub>4</sub> KY. ....	S12
<b>Table S1</b> The dimensional detail of the L-HFs assembly. ....	S13
<b>Figure S4</b> TEM image of self-assembly of F <sub>4</sub> KY at different pH in phosphate buffer. ....	S14
15.2 Characterization of L-HFs self-assembly of F <sub>4</sub> KY .....	S15
<b>Figure S5</b> The HT voltage curve and absorbance corresponding to the red CD profiles in Figure 1e.....	S15
<b>Figure S6</b> Assigned <sup>1</sup> H chemical shifts of F <sub>4</sub> KY in L-HFs. ....	S16
<b>Figure S7</b> <sup>1</sup> H NMR spectrum of L-HFs self-assembly of F <sub>4</sub> KY .....	S17
<b>Figure S8</b> <sup>1</sup> H- <sup>1</sup> H TOCSY of L-HFs self-assembly of F <sub>4</sub> KY .....	S18
<b>Table S2</b> The correlation list of chemical shifts according to <sup>1</sup> H- <sup>1</sup> H TOCSY in Figure S8. ....	S19
<b>Figure S9</b> <sup>1</sup> H- <sup>1</sup> H COSY of L-HFs self-assembly of F <sub>4</sub> KY .....	S20
<b>Table S3</b> The correlation list of chemical shifts according to <sup>1</sup> H- <sup>1</sup> H COSY in Figure S9.....	S21
<b>Figure S10</b> NOESY of L-HFs self-assembly of F <sub>4</sub> KY .....	S22
15.3 Molecular dynamics (MD) simulation of the L-HFs self-assembly of F <sub>4</sub> KY .....	S23
15.4 Discussion about the parallel β-sheets in L-HFs .....	S23
<b>Figure S11</b> Molecular dynamics simulation of F <sub>4</sub> KY into L-HFs.....	S25
<b>Figure S12</b> MD results of parallel β-sheet and anti-parallel β-sheet self-assembly of F <sub>4</sub> KY. ....	S26

<b>Table S4</b> Binding free energy ( $\Delta G$ ) in kcal/mol to compare the stability of parallel and anti-parallel $\beta$ -sheet in stacking for formation of the helical structure. ....	S27
<b>Figure S13</b> Relative distance of the MD results of amide protons between F1-F2 and F2-F3, between F1-F2 and K-Y, respectively, within the parallel $\beta$ -sheet plane. ....	S28
<b>Figure S14</b> MD results showing the $\pi$ - $\pi$ stacking in the L-HFs self-assembly of F <sub>4</sub> KY. ....	S29
<b>Figure S15</b> MD results showing the polar zipper in the L-HFs self-assembly of F <sub>4</sub> KY. ....	S30
16. Furin-instructed L-HFs self-assembly of F <sub>4</sub> KY .....	S31
<b>Figure S16</b> Schematic illustration of the furin cleavage and L-HFs transformation process of acetyl-RVRRF <sub>4</sub> KY nanoparticles. ....	S31
<b>Figure S17</b> Photographs showing the furin-catalyzed cleavage of acetyl-RVRRF <sub>4</sub> KY and L-HFs self-assembly of F <sub>4</sub> KY. ....	S32
<b>Figure S18</b> HPLC results of the furin cleavage products of Ac-RVRRF <sub>4</sub> KY .....	S33
<b>Figure S19</b> MALDI-TOF mass spectra of Ac-RVRRF <sub>4</sub> KY solution after 6 h furin cleavage... ..	S34
<b>Figure S20</b> The membrane disruption ability of furin-instructed L-HFs self-assembly of F <sub>4</sub> KY and its analogues inside MLV, monitored using encapsulated calcein as the indicator .....	S35
<b>Figure S21</b> TEM images of MLV without in situ self-assembly .....	S36
<b>Figure S22</b> The Young's modulus of L-HFs of F <sub>4</sub> KY and its analogues .....	S37
<b>Figure S23</b> The modulus test map of L-HFs self-assembly of F <sub>4</sub> KY and its analogues .....	S38
17 MD simulation of the interaction between L-HFs self-assembly of F <sub>4</sub> KY and membrane.....	S39
<b>Figure S24</b> The MD simulation showing the biomembrane penetration process by L-HFs self-assembly of F <sub>4</sub> KY .....	S40
<b>Figure S25</b> MD results showing the change of bending angle of the L-HFs self-assembly in the membrane. ....	S41
<b>Figure S26</b> MD results showing the change of the channel diameter inside the POPC bilayers membrane with the increasing of the interaction time of the L-HFs self-assembly of F <sub>4</sub> KY with the membrane. ....	S42
18. TfR, C <sub>6</sub> , and furin-instructed L-HFs self-assembly of F <sub>4</sub> KY in the Golgi of cancer cells .....	S43
18.1 Precursor design for cell uptake and targeting of the Golgi of cancer cells .....	S43
<b>Figure S27</b> TfR recognition by C <sub>6</sub> .....	S44
<b>Figure S28</b> Cell viability of FAM-C <sub>4</sub> R, FAM-C <sub>5</sub> R, FAM-C <sub>6</sub> R, FAM-C <sub>7</sub> R, and FAM-C <sub>8</sub> R after 24 h of incubation with MCF-7 cells .....	S45
<b>Figure S29</b> Pearson's correlation factor of fluorescent polycysteine and Bodipy ceramide in MCF-7 cells after 4 h of incubation .....	S46
18.2 Cancer cell Golgi apparatus targeting ability of C <sub>6</sub> R .....	S47
<b>Figure S30</b> Fluorescence images of FAM-C <sub>6</sub> R in incubation with cancer cells .....	S47
<b>Figure S31</b> Co-localization of FAM-C <sub>6</sub> R and Golgi-RFP in MCF-7 cell.....	S48
<b>Figure S32</b> Immunofluorescence image of the Golgi. ....	S49
<b>Figure S33</b> Pearson's correlation factor between FAM-C <sub>6</sub> R and Bodipy ceramide in different cell lines as a function of incubation time .....	S50

18.3 The L-HFs self-assembly of F <sub>4</sub> KY in the Golgi of cancer cells.....	S51
<b>Figure S34</b> The influence of different inhibitors on the cellular uptake of C <sub>6</sub> RVRRF <sub>4</sub> KY.....	S51
<b>Figure S35</b> Cyclic voltammetric curves of FAM-C <sub>6</sub> R and cysteine at pH 6.2 and 6.7.....	S52
<b>Figure S36</b> HPLC results of the furin cleavage products of C <sub>6</sub> RVRRF <sub>4</sub> KY.....	S53
<b>Figure S37</b> The MALDI-TOF mass spectra of C <sub>6</sub> RVRRF <sub>4</sub> KY solution after 6 h furin .....	S54
<b>Figure S38</b> Illustration of the structure of C <sub>6</sub> (K <sup>Dab</sup> )RVRR(K <sup>Dan</sup> )F <sub>4</sub> KY and its cleavage products. .....	S55
<b>Figure S39</b> Optical and fluorescence images of C <sub>6</sub> (K <sup>Dab</sup> )RVRR(K <sup>Dan</sup> )F <sub>4</sub> KY before and after introducing furin.....	S56
<b>Figure S40</b> Furin-instructed cleavage of C <sub>6</sub> (K <sup>Dab</sup> )RVRR(K <sup>Dan</sup> )F <sub>4</sub> KY (31±16 nm) and self- assembly of fluorescent (K <sup>Dan</sup> )F <sub>4</sub> KY .....	S57
<b>Figure S41</b> The fluorescence image of the self-assembly of fluorescent (K <sup>Dan</sup> )F <sub>4</sub> KY after furin- instructed cleavage of C <sub>6</sub> (K <sup>Dab</sup> )RVRR(K <sup>Dan</sup> )F <sub>4</sub> KY .....	S58
<b>Figure S42</b> Furin-instructed cleavage of C <sub>6</sub> (K <sup>Dab</sup> )RVRR(K <sup>Dan</sup> )F <sub>4</sub> KY monitored by fluorescence spectra at different time after introducing furin.....	S59
<b>Figure S43</b> Flow cytometry histograms of cancer and normal cell lines that were incubated with C <sub>6</sub> (K <sup>Dab</sup> )RVRR(K <sup>Dan</sup> )F <sub>4</sub> KY.....	S60
<b>Figure S44</b> Flow cytometry gating strategy used in the Figure S43 .....	S61
<b>Figure S45</b> The influence of furin inhibitor on peptide cleavage .....	S62
<b>Figure S46</b> The MALDI-TOF mass spectra of MCF-7 cell extract after 4 h incubation with C <sub>6</sub> (K <sup>Dab</sup> )RVRR(K <sup>Dan</sup> )F <sub>4</sub> KY.....	S63
<b>Figure S47</b> The MALDI-TOF mass spectra of MCF-7 cell extract after 4 h incubation with C <sub>6</sub> RVRRF <sub>4</sub> KY .....	S64
<b>Figure S48</b> Immunofluorescence image of cis-Golgi or trans-Golgi when MCF-7 cells were incubated by C <sub>6</sub> (K <sup>Dab</sup> )RVRR(K <sup>Dan</sup> )F <sub>4</sub> KY .....	S65
<b>Figure S49</b> Light scattering spectra of F <sub>4</sub> KY at different concentrations and the relationship between scattering intensity and concentrations .....	S66
<b>Figure S50</b> TEM images of furin-instructed L-HFs self-assembly in the Golgi after 24 h incubation of C <sub>6</sub> RVRRF <sub>4</sub> KY with MCF-7 cells.....	S67
<b>Figure S51</b> TEM images the nucleus, cell membrane, lysosomes, mitochondria and endoplasmic reticulum of MCF-7 cells after 4 h of incubation with C <sub>6</sub> RVRRF <sub>4</sub> KY .....	S68
<b>Figure S52</b> Images of MCF-7 cells at different time and different magnification after incubation with C <sub>6</sub> RVRRF <sub>4</sub> KY.....	S69
<b>Figure S53</b> The MCF-7 cells cytotoxicity data of F <sub>4</sub> KY peptide with different concentration after 24 h incubation. ....	S70
<b>Figure S54</b> Principal component analysis of the cytokine secretion .....	S71
Appendix 1 Mass spectrometric analysis of peptides.....	S72
SI References .....	S81

## 1. Instruments and materials

High-resolution transmission electron microscopy (HRTEM) images were recorded with Transmission Electron Microscope JEM-2100F (JEOL, Japan) and Tecnai G2 F20 S-TWIN microscopy (FEI, USA). The height of the assembly was recorded in air with AFM-SmartSPM (Horiba, Japan) in the AC mode; the probe was HQ: NSC14/Al BS, 160kHz, 5.0N/m. A Jasco J-810 spectropolarimeter (JASCO, Japan) was used for recording circular dichroism (CD) spectra. An FTIR-4800 Fourier transform infrared (FTIR) spectrophotometer (Shimadzu, Japan) was used to record IR spectra. UV-visible Absorption spectra were scanned with a UV-1800 spectrophotometer (Shimadzu, Japan). Powder X-ray diffraction (XRD) spectra were recorded with a D8 Advance (Bruker, Germany). *In vivo* fluorescence images were acquired using IVIS Spectrum (PerkinElmer, USA). Fluorescence spectra were scanned with a F2500 spectrophotometer (Hitachi, Japan). Fluorescence microscopic images were acquired using an Olympus IX-81 inverted microscope equipped with an Olympus IX2-DSU confocal scanning system (Olympus, Japan) and a Rolera-MGi EMCCD (QImaging, America). The mass spectra were acquired using MALDI-TOF/TOF Mass Spectrometer (AB Sciex 5800).

All the peptides in this work were designed by our group, synthesized and mass spectrometrically analysed by Sangon Biotech (Shanghai) Co., Ltd. All other chemicals were of analytical reagent and purchased from Sigma-Aldrich Company Ltd. The following primary antibodies were used for western blotting. All the antibodies were diluted and used following the supplier protocol.

Anti-GBF1, Abcam, catalog: #ab86071;

Anti-GALT (G1), Santa Cruz Biotechnology, catalog: #sc-365577;

Anti-Actin, Abcam, catalog: #ab179467;

The following primary antibody was used for immunofluorescence.

Cytochrome C monoclonal antibody (FITC labelled), ThermoFisher, catalog: #11-6601-82;

Anti-BAX, Abcam, catalog: #ab192819;

Anti-GM130, Abcam, catalog: #ab52649;

Anti-TGN 46, Abcam, catalog: #ab50595;

Secondary Antibody, Goat Anti-Rabbit IgG-H&L (Cy3®), Abcam, catalog: #ab6939.

## 2. Peptide self-assembly in aqueous medium

F<sub>4</sub>KY (8.98 mg) was first dissolved in 1 mL of hexafluoroisopropanol (HFIP) and the resulted solution was sit for 4 h at room temperature. And 2 mL of Milli-Q water (or PBS) was added. The peptide HFIP-water solution was placed in a fume hood at 25 °C for 5 d to allow natural evaporation to remove HFIP. After evaporation, Milli-Q water was added to the peptide solution to bring the volume to 2 mL. The resulted peptide solution was then incubated at 25 °C for 5 d without disturbance and the F<sub>4</sub>KY hydrogel was observed.

For AFM and TEM characterization, a rapid sample preparation procedure was adopted. The characterization results of the hydrogel fibrils and rapid preparation fibrils are not affected by the rapid procedure. F<sub>4</sub>KY (0.98 mg) was first dissolved in 200 µL of HFIP to prepare a 5 mM peptide solution. After 4 h, 20 µL of the 5 mM peptide HFIP solution was added to 80 µL of Milli-Q water (1 mM). After 20 min, 900 µL of Milli-Q water was added to make a 100 µM peptide solution. After another 20 min, the peptide solution was diluted to 20 µM by adding 4 mL of Milli-Q water. Then, 3 µL of the 20 µM peptide solution was applied onto the copper mesh with carbon support

film. With the evaporation of the solvent at ambient temperature (~25 °C), the concentration of F<sub>4</sub>KY would increase and self-assemble occur and deposit on the carbon supporting film of copper mesh. After 4 h evaporation, the copper mesh with F<sub>4</sub>KY self-assembly was directly used for TEM measurements. For AFM measurements, 10 µL of the 20 µM peptide solution was added on the mica slide and the same evaporation procedure was followed.

In the furin-instructed self-assembly, 300 µM peptide precursors were mixed with furin (5 U) (ab126908, Abcam) in 4-(2-hydroxyethyl)-1-piperazineethanesulfonic acid (HEPES) buffer (pH 7.5) and then kept at 37°C for 24 h. The HEPES buffer was used in the furin cleavage experiments to maintain the better enzymatic activity of furin in test-tube.

### **3. Multilamellar vesicle (MLV) preparation**

Lecithin (19.8 mg), cholesterol (4.7 mg), and DSPE-PEG 2000 (7.6 mg) were dispersed in 1.5 mL of chloroform and transferred to a round bottom flask. After removal of chloroform by rotary evaporator at 40 °C, materials on the bottle wall were further dried in the vacuum oven at room temperature for 4 h. Subsequently, 1 mL of HEPES buffer was added to this flask, and the MLV was produced at room temperature by repeatedly pipetting the solution 50 times. For encapsulation, assembly precursors (3 mg) and furin (20 U) were dissolved in the HEPES buffer and added to the flask after rotary evaporation. With centrifuging at 5000 rpm for 5 min, the supernatant was discarded to remove the unencapsulated species.

### **4. TEM study of L-HFs self-assembly of F<sub>4</sub>KY in the Golgi and MLV**

Cells grown in cell culture flasks were incubated with C<sub>6</sub>RVRRF<sub>4</sub>KY. Cells were washed and fixed in 4% glutaraldehyde at 0 h, 4 h, 8 h, and 24 h, respectively. After washing with 10 mM PBS, cells were treated with 0.5 % OsO<sub>4</sub> for 1 h at 4 °C. Cells were then rinsed with Milli-Q water and stained with saturated uranyl acetate in 70% ethanol for 24 h at room temperature. Subsequently, cells were dehydrated in 99.9% ethanol and then embedded in Epon™ resin. Thin (70 nm) sections were obtained with an ultramicrotome. Electron micrographs were obtained with a transmission electron microscope. MLV were also treated following the same procedure as described above.

### **5. Quantification of cytokines**

MCF-7 cells were treated with Ac-RVRR, C<sub>6</sub>RVRR, F<sub>4</sub>KY, Ac-RVRRF<sub>4</sub>KY, or C<sub>6</sub>RVRRF<sub>4</sub>KY, respectively. After 6 h of incubation, supernatant was collected and submitted for analysis by means of a bead-based multiplex assay using the Milliplex Map Kit (Merck Millipore) and Luminex technology according to the manufacturer's instructions. Briefly, 30 µL of each sample, controls, and standards were added to a plate, respectively. Antibody-labelled fluorescent beads were then added and incubated overnight at 4°C. Wells were washed and biotinylated detection antibodies were added. After 1.5 h at room temperature, streptavidin-phycoerythrin was added. And the resulted solution was kept at room temperature for 1 h. Finally, wells were washed and fluorescence intensities were obtained with a FlexMap 3D. The average of triplicates was calculated in a data set of 20 parameters for four conditions. The data was centered and scaled to unit variance and subjected to principal component analysis (PCA) with IBM SPSS Statistics 22, which explains 64% of total inertia.

## 6. *In vivo* imaging and treatment study

All animal experiments were in accordance with protocols No.SYXK 2019-0005, which was approved by the Animal Use and Care Administrative Advisory Committee at the Chongqing University. The subcutaneous MCF-7 tumor model was developed by injection of  $1 \times 10^6$  MCF-7 cells into the back of the nude mice. The tumor-bearing mice were randomly assigned to three groups (five mice at each point). For treatment, PBS or C<sub>6</sub>RVRRF<sub>4</sub>KY were injected via the tail vein once a day over a period of 14 d. For *in vivo* imaging, C<sub>6</sub>K<sup>Dab</sup>RVRRK<sup>Dan</sup>F<sub>4</sub>KY were injected via the tail vein. The cleavage and self-assembly of peptides were monitored using an *in vivo* fluorescence imaging system (ISIV Lumina, Perkin Elmer) at the predetermined time. Mice were sacrificed at the endpoint of treatment. The tumors and major organs were harvested, weighed, and fixed with 4% paraformaldehyde for *in vitro* imaging and further hematoxylin-eosin (H&E) staining of tissue sections. The body weight was monitored throughout the study and the tumor volume was estimated by the following formula:

$$V = (L \times W^2)/2$$

## 7. Cell viability test and fluorescence imaging

The  $1 \times 10^5$  cell/mL cells suspended in dulbecco's modified eagle medium (DMEM) supplemented with 10% fetal bovine serum (FBS) were added to a 96-well plate (100  $\mu$ L per well). After 24 h incubation (37 °C, 5% CO<sub>2</sub>), the cell culture medium was replaced by DMEM supplemented with 2% FBS which contains different doses of F<sub>4</sub>KY or assembly precursors. After another 24 h incubation (37 °C, 5% CO<sub>2</sub>), cells were washed with HEPES buffer, then, a mixture of Cell Counting Kit-8 (CCK-8, 10  $\mu$ L) and DMEM (90  $\mu$ L) was added to each well. The optical density (OD) in each well was measured at 450 nm with a microplate reader. The cell viability was estimated according to the equation:

$$\text{Cell viability [\%]} = (\text{OD peptide}/\text{OD control}) \times 100\%$$

Before fluorescence imaging, cells were cultured on the surface of glass bottom dishes. Incubation conditions for fluorescence imaging were the same as that for the cell viability test. After 4 h incubation with peptides, cells were washed three times with phosphate buffered saline (PBS) and observed with a confocal microscope with illumination and detector described in the Supporting Information.

The primary antibody was anti-BAX (ab192819, Abcam) and the secondary antibody was Goat Anti-Rabbit IgG–H&L (Cy3®) (ab6939, Abcam) in Bax imaging experiments. Cytochrome c monoclonal antibody (FITC labelled) (11-6601-82, ThermoFisher) was used in Cytochrome c imaging experiments. The primary antibody anti-GM130 (ab52649, Abcam) and anti-TGN 46 (ab50595, Abcam) were used in *cis*-Golgi and *trans*-Golgi immunofluorescence imaging experiments, respectively, and the secondary antibody was Goat Anti-Rabbit IgG–H&L (Cy3®) (ab6939, Abcam).

## 8. Flow cytometry

Before flow cytometric measurements, cells were cultured on the surface of glass bottom dishes. Incubation conditions for flow cytometric measurements were the same as that for the cell viability test. After 4 h incubation of the cells with C<sub>6</sub>(K<sup>Dab</sup>)RVRR(K<sup>Dan</sup>)F<sub>4</sub>KY, cells were washed three times with PBS and digested by trypsin for 1 min. After detachment from the glass bottom dishes, cells were collected by centrifugation at 1200 rpm for 3 min, and then suspended in PBS for flow cytometry.

## 9. Sample preparation for MALDI-TOF-MS

MCF-7 cells were treated with C<sub>6</sub>(K<sup>Dab</sup>)RVRR(K<sup>Dan</sup>)F<sub>4</sub>KY or C<sub>6</sub>RVRRF<sub>4</sub>KY. After 4 h of incubation (37 °C, 5% CO<sub>2</sub>), cells were washed three times with PBS and digested by trypsin for 1 min at 37 °C. After detachment from the glass bottom dishes, cells were collected by centrifugation at 1200 rpm for 3 min, and then washed by PBS and suspended in methanol (1× 10<sup>6</sup> cell/mL). Then, the cells were added in a glass homogenizer and homogenized in methanol at 4 °C for 3 minutes. After homogenization, the cells were sonicated at 0 °C for 5 minutes and then placed at -20 °C for 20 minutes, repeated three times. The methanol supernatant was collected by centrifugation at 14000 rpm for 3 min. Before being used for MALDI-TOF-MS testing, the methanol cell extracts are stored at -80 °C. α-Cyano-4-hydroxycinnamic acid (HCCA) was used as the matrix.

## 10. NMR methods

The NMR samples were prepared in PBS (pH 7.0, 10 mM). D<sub>2</sub>O (10 %) was added into the samples and 2,2-dimethyl-2-silapentanesulfonic acid (DSS) was also added as the internal chemical shift reference. The final F<sub>4</sub>KY concentration for NMR experiments was 500 μM. The NMR experiments were performed at 25°C on Bruker Avance 700 MHz and 800 MHz spectrometers equipped with four RF channels and triple-resonance cryoprobes with pulsed field gradients. The chemical shift assignments of backbone and side-chain atoms were obtained by two-dimensional (2D) HCCH-COSY and HCCH-TOCSY experiments. 2D <sup>1</sup>H-<sup>1</sup>H NOESY spectra were collected to confirm the NOE effect. The NMR spectra were processed using NMRPipe (Delaglio *et al.* 1995)<sup>1</sup> and analysed by NMRView (Johnson and Blevins 1994)<sup>2</sup>.

## 11. Simulation methods for F<sub>4</sub>KY self-assembly

In molecular dynamics simulations, the ff14SB force field and explicit solvent of TIP3P were employed to perform MD simulations in the Amber18 package<sup>3-4</sup>. The distance between the box edge and the short peptide is more than 1.2 nm. The SHAKE algorithm was applied to constrain bonds such as π-π stacking and hydrogen bonding. The particle mesh Ewald summation method was used to describe long-range electrostatic interactions. The cutoff distance of non-bond interactions is 1.0 nm. The Berendsen barostat and Langevin thermostat was used to control the temperature in the current study. A 500 ns trajectory was collected for each system, and the last 100 ns equilibrated data were used for further analysis. The MD data were processed with VMD 1.9.3 OpenGL Display.

## 12. Simulation methods for the interaction between L-HFs self-assembly and membrane

The ideal fibrils composed of parallel β-sheets were prepared by antechamber module (in Amber 18) and Visual Molecular Dynamics (VMD) software. 120 F<sub>4</sub>KY molecules were used to assemble into a left-handed fibril with an effective width, length and height of 4.8 nm, 13.2 nm and 2.1 nm, respectively. The POPC (1-palmitoyl-2-oleoyl-sn-glycero-3-phosphocholine) type membrane was derived from the module of Membrane Builder in CHARMM-GUI<sup>5</sup>. A 100 Å×100 Å membrane was used for study with a greater than 1.2 nm distance between the peptides and box edge to avoid the edge effect. The 0.15 M KCl was used in the fibril-membrane complex system. The ideal straight fibril was aligned along Z axis, perpendicular to the membrane plane. In MD simulations, the force field of ff14SB<sup>3</sup>, lipid17, and TIP3P was employed to describe the peptides, lipid, and water, respectively, with the



Amber18 package<sup>4</sup>. The SHAKE algorithm was applied to constrain hydrogen bonds. The particle mesh Ewald summation method was used to describe long-range electrostatic interactions. The cutoff distance is 1.0 nm for non-bond interactions. The temperature controlled by the Langevin thermostat and Berendsen barostat was used in the current study. A 500 ns trajectory was collected for each system.

### **13. Statistical analysis**

Data are presented as mean  $\pm$  s.d. One-way analysis of variance (ANOVA) was used for multiple-group comparison. Intergroup comparison was analysed by Student's *t*-test (two-tailed). \* means  $p < 0.05$ , \*\* means  $p < 0.01$  and \*\*\* means  $p < 0.001$ .

#### 14. Chemical structure of C<sub>6</sub>RVRRF<sub>4</sub>KY

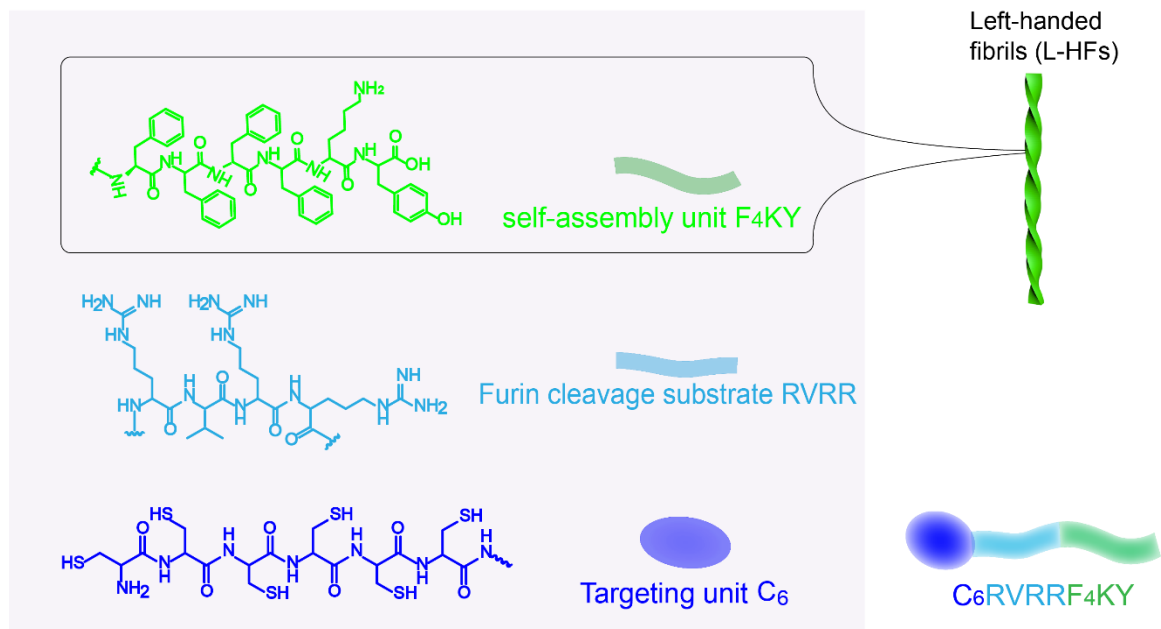


**Figure S1** Chemical structure of three different functional units of C<sub>6</sub>RVRRF<sub>4</sub>KY.

## 15. Morphology and mechanism of L-HFs self-assembly of F<sub>4</sub>KY

### 15.1 Self-assembly of F<sub>4</sub>KY

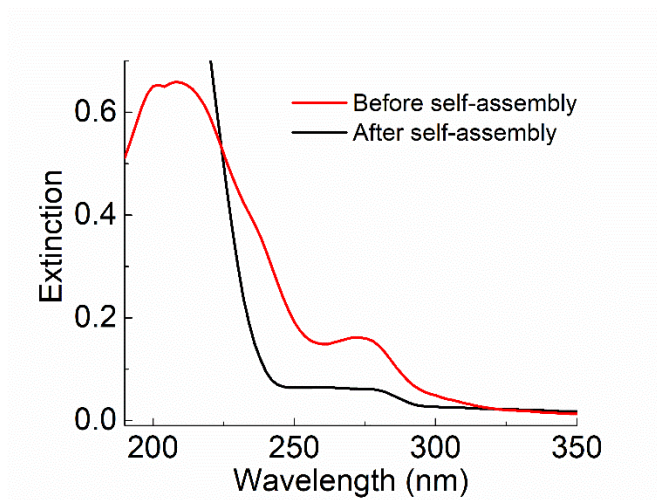


**Figure S2** Extinction spectra of F<sub>4</sub>KY before and after self-assembly. The extinction spectra before self-assembly were recorded by dissolving F<sub>4</sub>KY in HFIP. The extinction spectra after self-assembly were recorded after the formation of F<sub>4</sub>KY hydrogel in Milli-Q water. The spectra were obtained after solvent subtraction. Experiments were repeated three times.

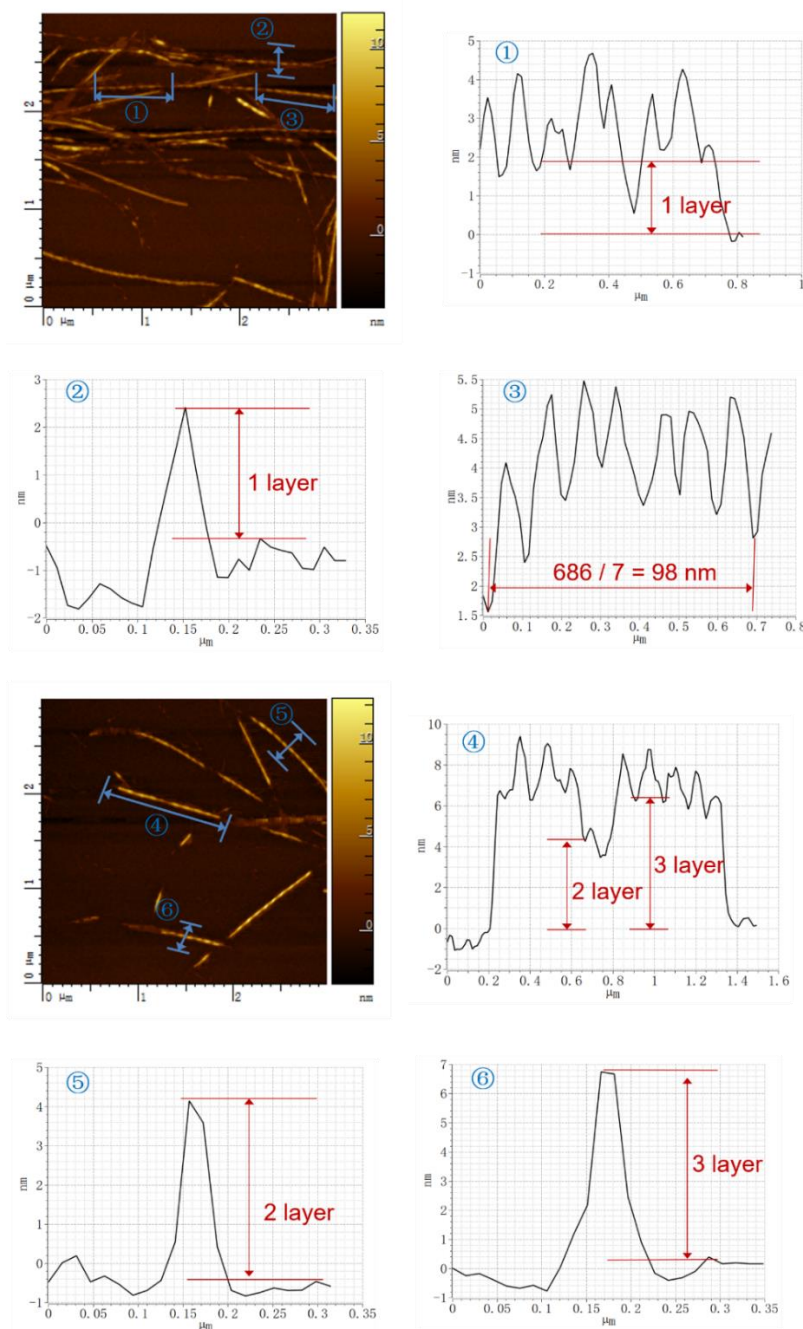


**Figure S3** Representative AFM images of left-handed helical fibrils (L-HFs) self-assembly of F<sub>4</sub>KY.

**Notes:** Results indicate that the L-HFs self-assembly of F<sub>4</sub>KY have a multi-layer structure composed of single-stranded L-HFs. More detail about the L-HFs self-assembly of F<sub>4</sub>KY can be seen in Table S1. The length of a single F<sub>4</sub>KY molecule is about 2.2 nm calculated by VMD software, which is in accordance with the height of the fibrils ( $2.2 \pm 0.3$  nm) measured by AFM. Experiments were repeated three times.

**Table S1** The dimensional detail of the L-HFs assembly.

Number of Layers	Period Length (nm)	Width (nm)	Height (nm)	Fraction (%)
1	$98 \pm 2$	$37 \pm 2$	$2.2 \pm 0.3$	21
2	$92 \pm 3$	$41 \pm 3$	$4.4 \pm 0.2$	44
3	$131 \pm 5$	$55 \pm 6$	$6.4 \pm 0.3$	8
>3	>131	>55	>6.4	27

**Notes:** Data were collected from AFM and TEM images of 100 nanofibrils. The periodic lengths and heights are calculated by the results of AFM measurements, and the width is calculated by the results of TEM measurements. Fraction is calculated as the number of occurrence divided by 100 which is the number of nanofibrils measured.

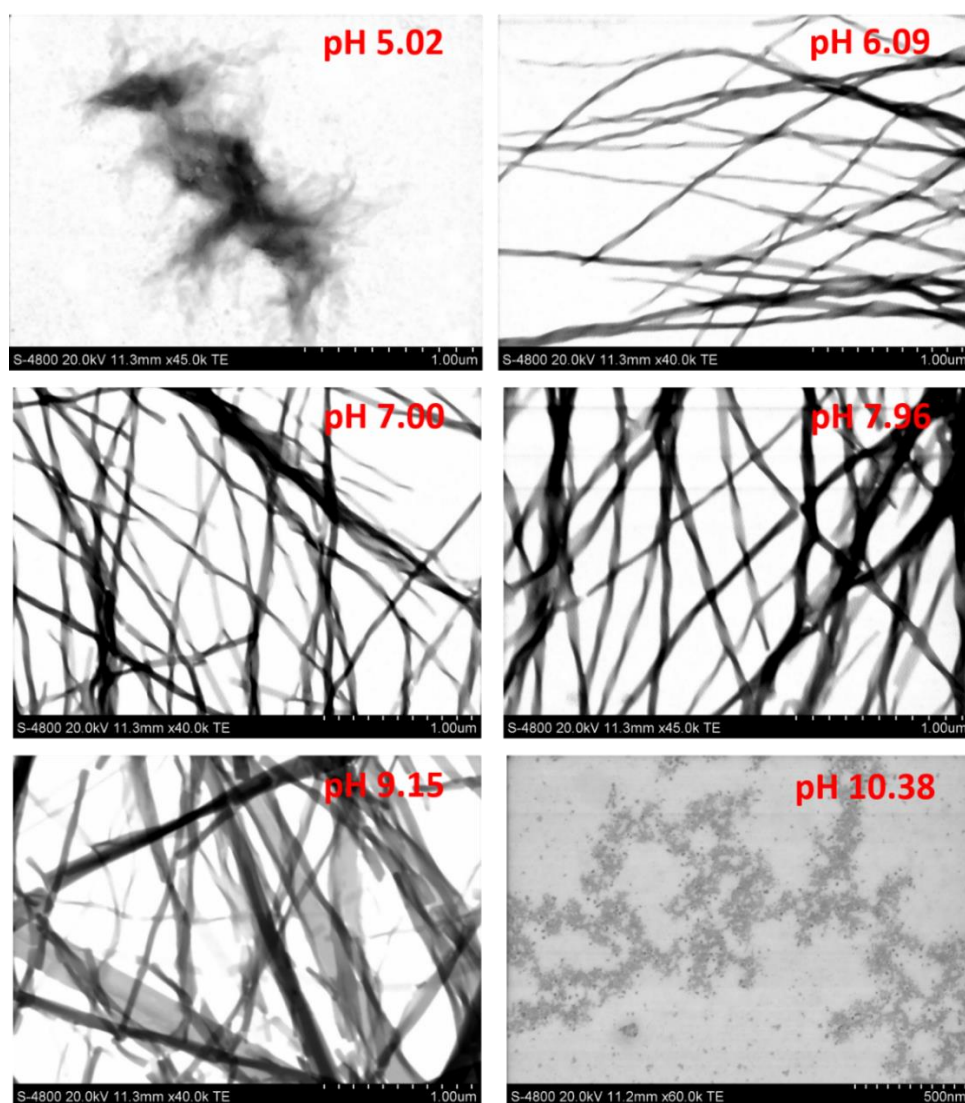


**Figure S4** TEM image of self-assembly of F<sub>4</sub>KY at different pH in phosphate buffer.

**Notes:** The helical fibrils of L-HFs self-assembly of F<sub>4</sub>KY occurred in aqueous medium with pH ranging from 6.09 to 9.15. The self-assembly may not occur in the lysosome, an important retrograde transport organelle with the pH usually lower than 5. Experiments were repeated three times.

## 15.2 Characterization of L-HFs self-assembly of F<sub>4</sub>KY

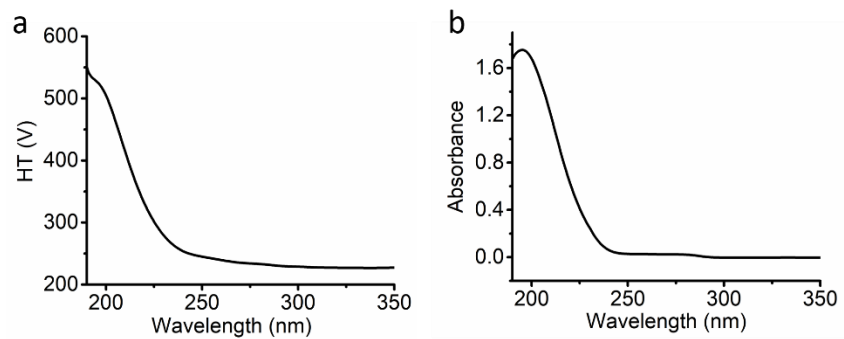


**Figure S5** The HT voltage curve (a) and absorbance (b) corresponding to the red CD profiles in Figure 1e.

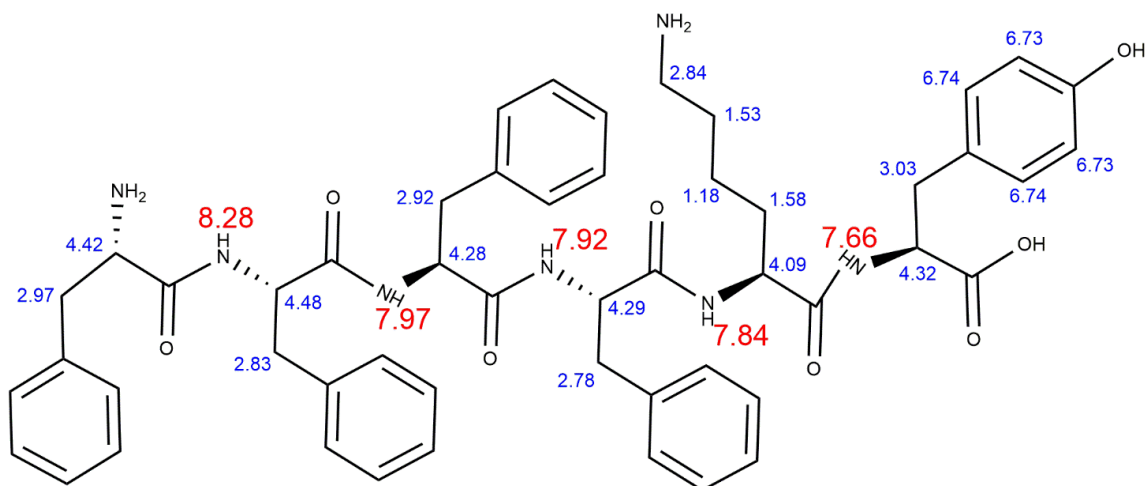


**Figure S6** Assigned  $^1\text{H}$  chemical shifts of F<sub>4</sub>KY in L-HFs.

**Notes:** The chemical shifts of the individual amino acid residue were determined by  $^1\text{H}$  NMR spectrum and assigned based on Correlation Spectroscopy (COSY), Total Correlation Spectroscopy (TOCSY), and Nuclear Overhauser effect spectroscopy (NOESY).

The chemical shifts of the five amide protons of F<sub>4</sub>KY are from 7.6 to 8.4 in the short peptide. And one of the chemical shifts was first assigned to be the chemical shift of a specific amide proton; subsequently, COSY, TOCSY, and NOESY were used to verify the assignment. After several assignments and verifications, most of the chemical shift of protons can be well assigned.

The  $^1\text{H}$  NMR spectrum is provided in Figure S7. All the basic data of TOCSY, COSY, and NOESY are provided in Figures S8–S10, Table S2, and Table S3.



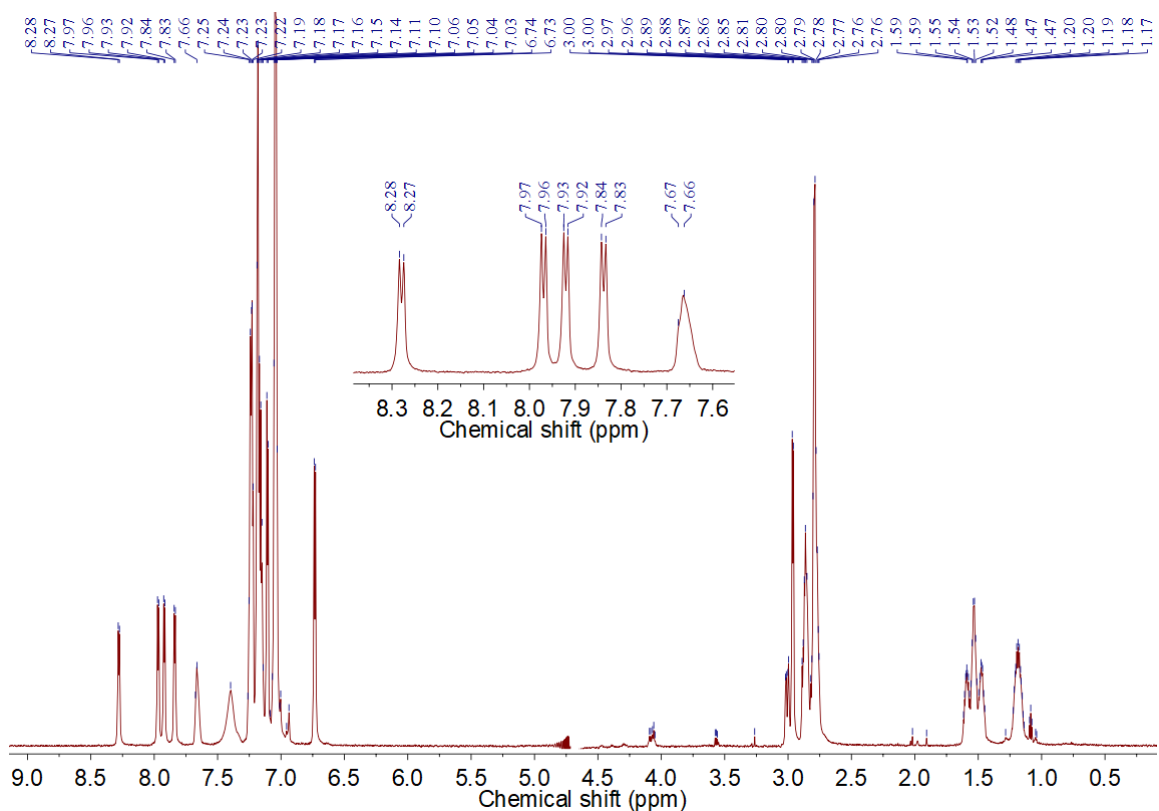


**Figure S7**  $^1\text{H}$  NMR spectrum of L-HFs self-assembly of F<sub>4</sub>KY. Insert: the magnified NMR spectrum from 7.6 ppm to 8.4 ppm presenting the chemical shifts of amide protons of F<sub>4</sub>KY. Experiments were repeated three times.

**Notes:** To obtain the NMR spectra of L-HFs self-assembly of F<sub>4</sub>KY with reasonable resolution for peak assignment, the concentration used in the NMR test is 500  $\mu\text{M}$ , a concentration higher than the critical aggregation concentration (110  $\mu\text{M}$ ) to assure the occurrence of self-assembly and well below the 5 mM gelatinization concentration which is easy to cause spectral overlap.

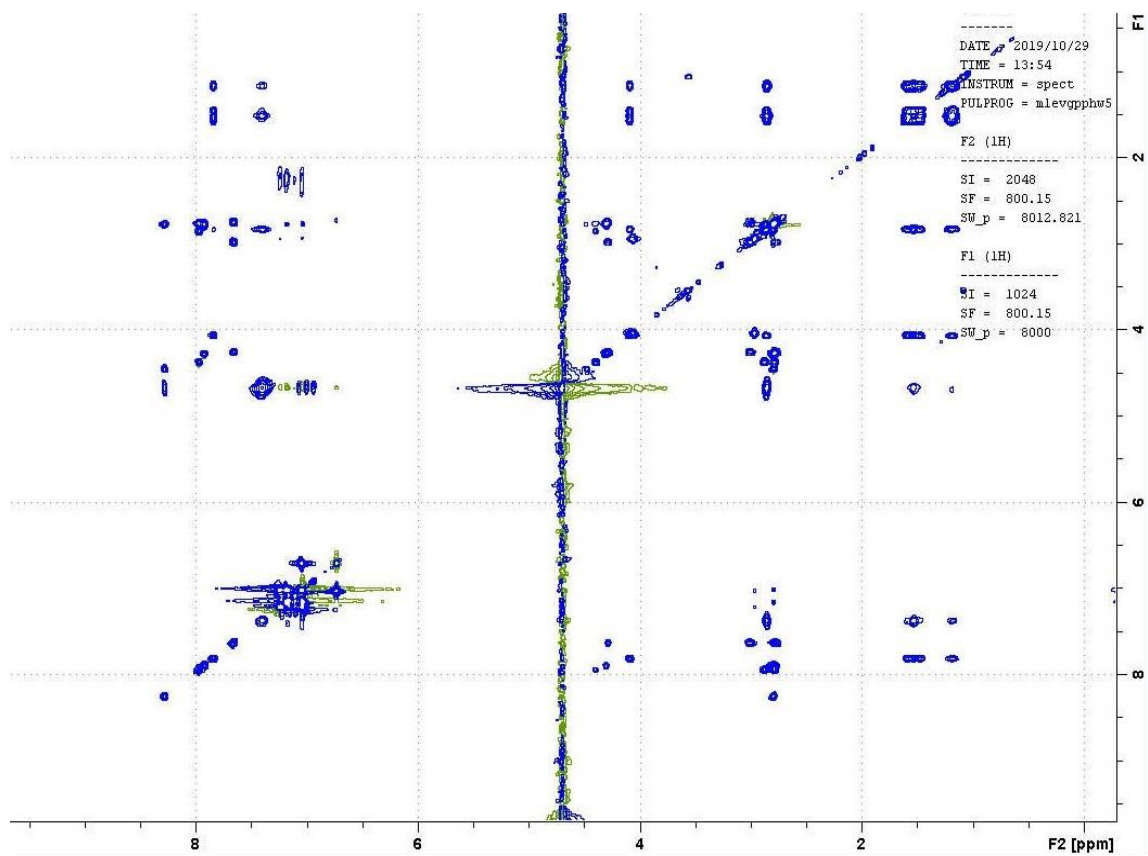


**Figure S8**  $^1\text{H}$ - $^1\text{H}$  TOCSY of L-HFs self-assembly of F4KY. Experiments were repeated three times.

**Table S2** The correlation list of chemical shifts according to  $^1\text{H}$ - $^1\text{H}$  TOCSY in Figure S8.

Number of total correlation group	Correlated chemical shift (ppm)						
1	4.42	2.97	-	-	-	-	-
2	8.28	4.48	2.83	-	-	-	-
3	7.97	4.28	2.92	-	-	-	-
4	7.92	4.29	2.78	-	-	-	-
5	7.84	4.09	2.84	1.58	1.53	1.18	
6	7.66	4.32	3.03				

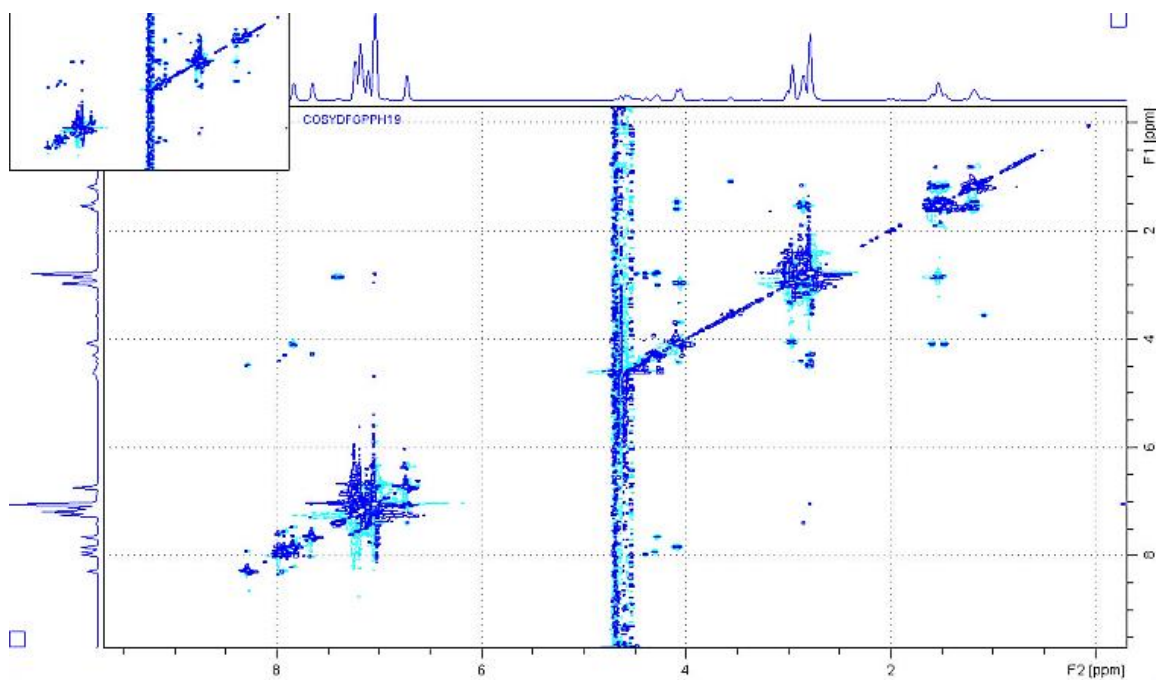


**Figure S9**  $^1\text{H}$ - $^1\text{H}$  COSY of L-HFs self-assembly of  $\text{F}_4\text{KY}$ . Experiments were repeated three times.

**Table S3** The correlation list of chemical shifts according to  $^1\text{H}$ - $^1\text{H}$  COSY in Figure S9.

Number of correlation group	Correlated chemical shift (ppm)	
1	4.42	2.97
2	8.28	4.48
3	4.48	2.83
4	7.97	4.28
5	4.28	2.92
6	7.92	4.29
7	4.29	2.78
8	7.84	4.09
9	4.09	1.58
10	1.58	1.18
11	1.18	1.53
12	1.53	2.84
13	7.66	4.32
14	4.32	3.03
15	6.74	6.73

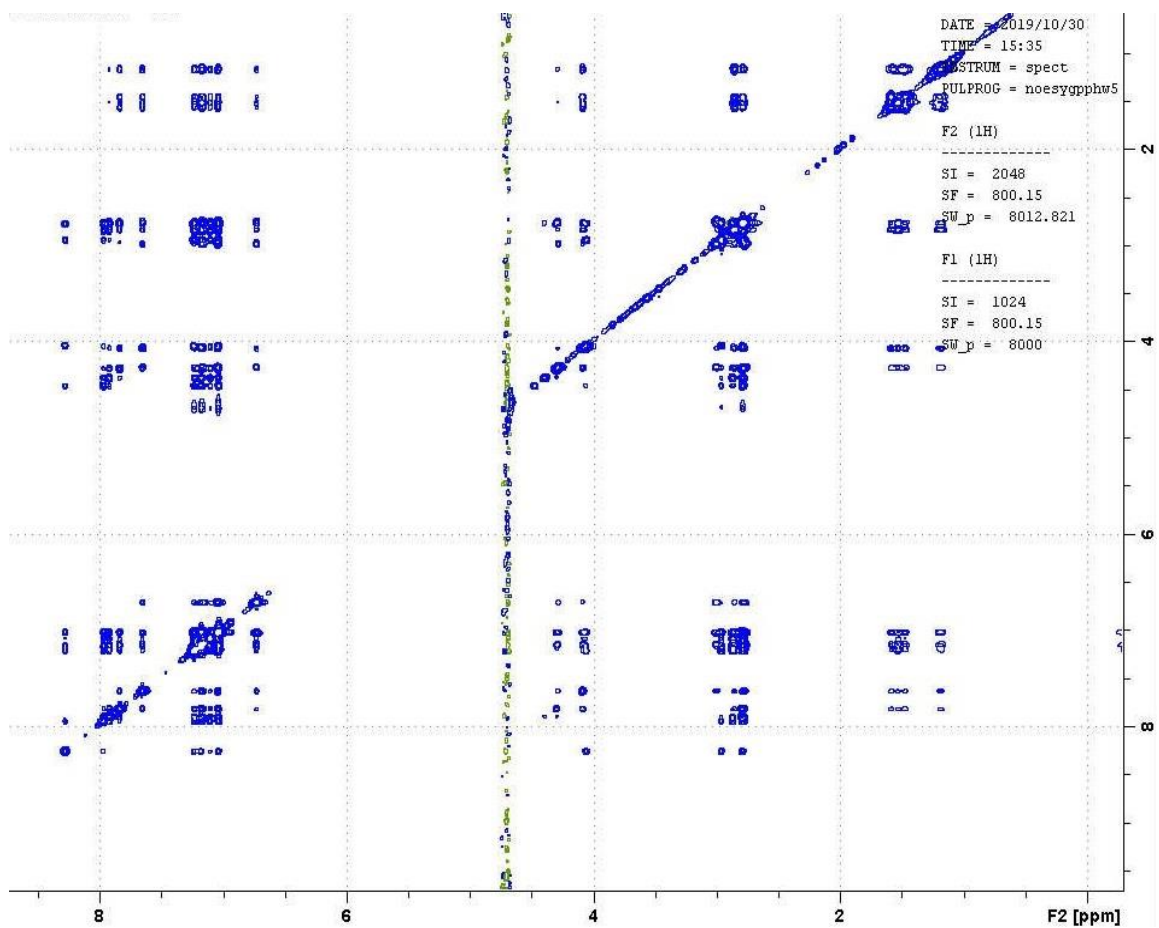


**Figure S10** NOESY of L-HFs self-assembly of F<sub>4</sub>KY. Experiments were repeated three times.

### 15.3 Molecular dynamics (MD) simulation of the L-HFs self-assembly of F<sub>4</sub>KY

The molecular dynamics simulation (Figures S11–S15), based on the ff14SB force field and explicit solvent of TIP3P in the Amber18 package, confirms the spectroscopic results and suggests that a helical structure forms by head-on-head stacking of parallel  $\beta$ -sheet planes, primarily via  $\pi$ - $\pi$  stacking and polar zippers along the helical axis (Figure 11). The simulated structure presents the spacing of 4.79 Å between  $\beta$ -strand backbones within the parallel  $\beta$ -sheet layer, spacing of 4.12 Å for  $\pi$ - $\pi$  stacking of benzene rings between  $\beta$ -sheet planes, and spacing of 10.09 Å between  $\beta$ -sheet planes, respectively, which agrees well with XRD measurements (Figure 1f). The MD simulation reveals that the F<sub>4</sub>KY parallel  $\beta$ -sheet is more stable than the anti-parallel  $\beta$ -sheet in the helical structure (Table S4), in which the  $\pi$ - $\pi$  stacking, polar zippers, and the left-handed twist of parallel  $\beta$ -sheets may provide additional assistance to stabilize the L-HFs self-assembly of F<sub>4</sub>KY<sup>6</sup>. Interestingly in the simulation, the left-handed twisted structure appears as the result of parallel  $\beta$ -sheet stacking, while the right-handed twisted structure appears as the result of anti-parallel  $\beta$ -sheet stacking (Figures S11–S15), with the former consistent with high-resolution transmission electron microscopic (HRTEM) and atomic force microscopic (AFM) measurements (Figure 1a–1c). The occurrence of parallel  $\beta$ -sheet stacking of L-HFs self-assembly produces the positively charged nitrogen terminal surface and negatively charged carbon terminal surface, respectively, along the fibrils (Figure S11 f). The oppositely charged surfaces may promote the interwinding of two helical assemblies to produce thick ones through the electrostatic attraction (Figure S11 f), which may be ascribed to the branched fibrous structure (Figure 1a–1b, Table S1).

### 15.4 Discussion about the parallel $\beta$ -sheets in L-HFs

The L-HFs self-assembly of the F<sub>4</sub>KY is an architecture basically composed of parallel  $\beta$ -sheets, which is different from the typical anti-parallel structure. The anti-parallel  $\beta$ -sheets are considered in most cases more stable than parallel  $\beta$ -sheets, because the lateral network of alternating hydrogen-bonded 10- and 14-membered rings in anti-parallel  $\beta$ -sheets is more stable than that of 12-membered rings in parallel  $\beta$ -sheets<sup>6-8</sup>. To address this issue, the energy difference of F<sub>4</sub>KY self-assembly based on the anti-parallel and parallel  $\beta$ -sheets, respectively, were interrogated by the molecular dynamics simulation (Figure S11). A sequence in the middle of a randomly selected

$\beta$ -sheet in the assembly was used to simulate the interaction with one of its adjacent sequence within the  $\beta$ -sheet plane and with sequences of the adjacent  $\beta$ -sheets along the axis, respectively (Figure S11). The interaction of the investigated sequence with the adjacent sequence within the  $\beta$ -sheet plane conforms to the usual expectation that anti-parallel  $\beta$ -sheet is more stable than the parallel  $\beta$ -sheet, because the hydrogen binding free energy is  $-29.45$  kcal/mol for the parallel  $\beta$ -sheet and  $-29.78$  kcal/mol for the anti-parallel  $\beta$ -sheet, respectively (Table S4). However, binding energy between the selected sequence and one of the adjacent  $\beta$ -sheet along the axis, which is be very important for formation of the fibrillar structure, is more favorable for parallel  $\beta$ -sheet formation with  $-2.63$  kcal/mol for the parallel configuration and  $0.41$  kcal/mol for the anti-parallel configuration, respectively (Figure S11). Furthermore, the MD simulation turns out that the anti-parallel  $\beta$ -sheets largely form the right-handed assembly with  $\beta$ -sheets loosely stacked; the parallel  $\beta$ -sheets form the more stable left-handed fibril assembly with ordered  $\beta$ -sheet stacking (Figure S11), which provide justification for the TEM, AFM, and NMR results (Figure 1a–1c and 1g). The  $\pi$ - $\pi$  stacking and polar zippers between  $\beta$ -sheet planes, as well as left-handed twist along the axis may provide additional support for stabilization of the F<sub>4</sub>KY self-assembly (Figure S11)<sup>6, 9</sup>.



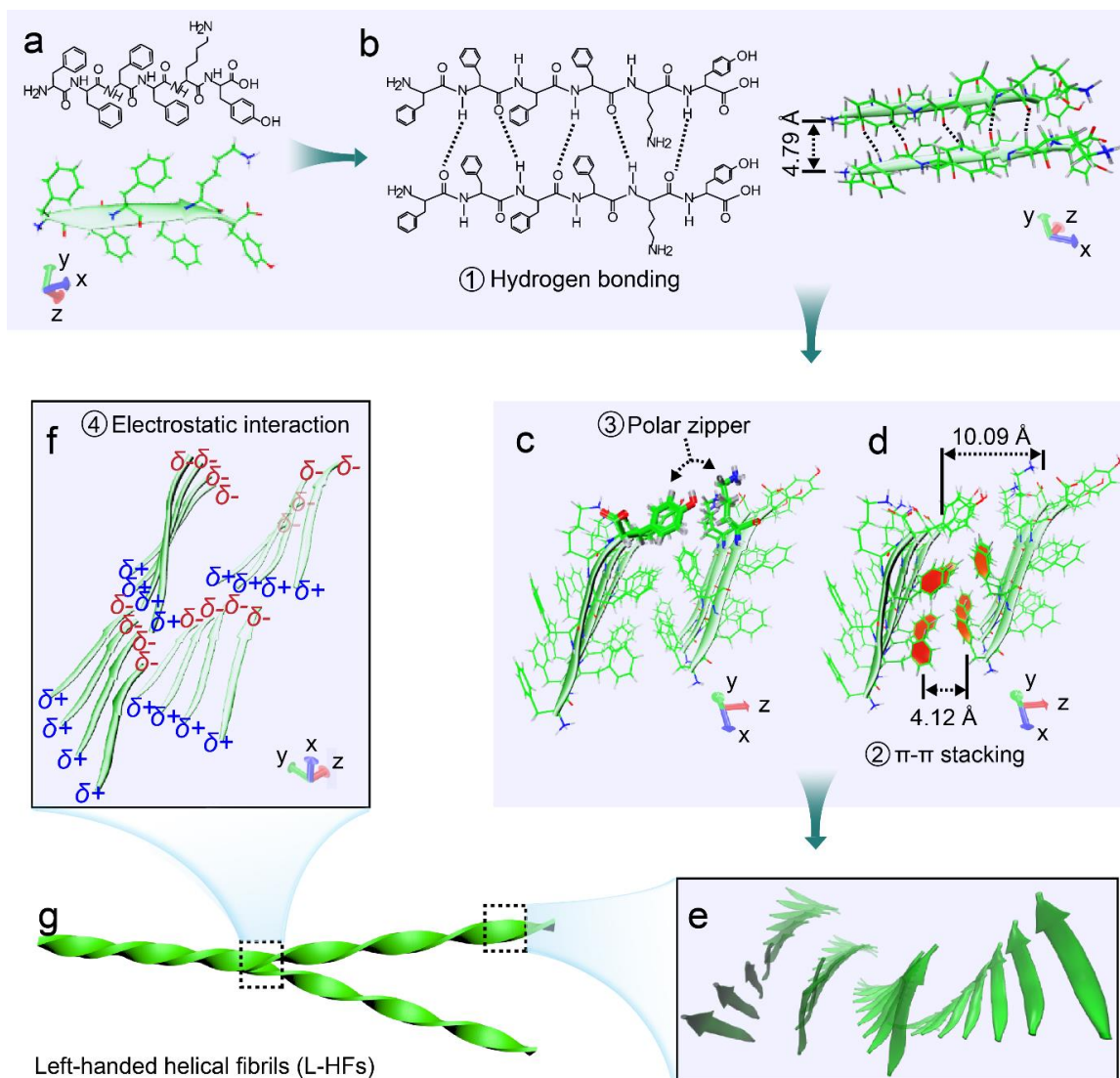
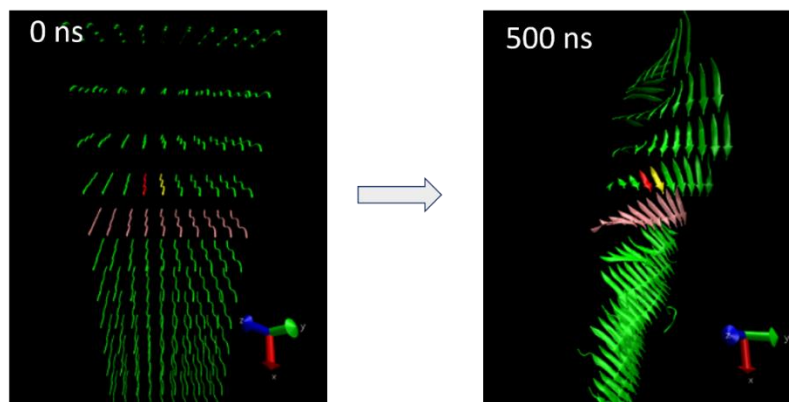


**Figure S11** Molecular dynamics simulation results showing the self-assembly process of F<sub>4</sub>KY into L-HFs. **a**, Molecular structure of F<sub>4</sub>KY. **b**, Parallel  $\beta$ -sheets promoted by hydrogen bonding between amide groups. **c** and **d**, Axial stacking of parallel  $\beta$ -sheets promoted by  $\pi$ - $\pi$  stacking and polar zipper. **e**, Single layered L-HFs of F<sub>4</sub>KY. **f**, Interwinding of two helical fibrils to produce a thick one through the electrostatic attraction. **g**, Illustration of L-HFs self-assembly of F<sub>4</sub>KY.

Parallel  $\beta$ -sheet  
stacking



Anti-parallel  $\beta$ -sheet  
stacking

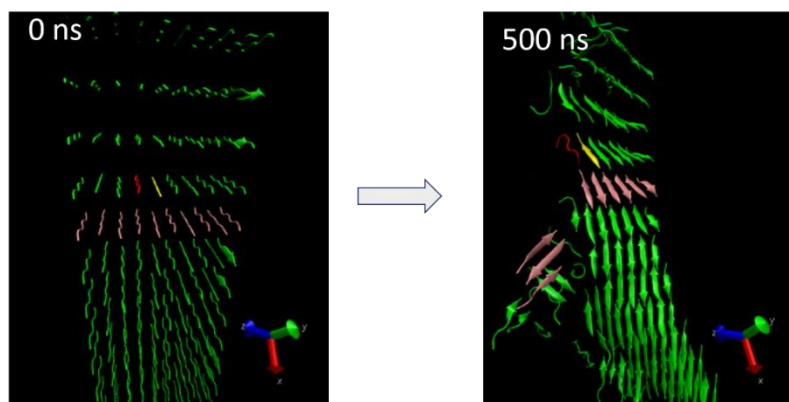


**Figure S12** MD results of parallel  $\beta$ -sheet (top row) and anti-parallel  $\beta$ -sheet (bottom row) self-assembly of F<sub>4</sub>KY. The strips represent short peptide F<sub>4</sub>KY.

**Table S4** Binding free energy ( $\Delta G$ ) in kcal/mol to compare the stability of parallel and anti-parallel  $\beta$ -sheet in stacking for formation of the helical structure.

With adjacent peptide within $\beta$ -sheet plane ( $\Delta G$ , kcal/mol) <sup>a</sup>		With adjacent $\beta$ -sheet plane ( $\Delta G$ , kcal/mol) <sup>b</sup>	
Parallel	Anti-parallel	Parallel	Anti-parallel
-29.4476	-29.7812	-2.6295	+0.4105

<sup>a</sup>:  $\Delta G$  between red and yellow peptides within the same  $\beta$ -sheet plane as shown in Figure S12.

<sup>b</sup>:  $\Delta G$  between red peptide and peptides in the adjacent  $\beta$ -sheet plane (highlighted in pink) as shown in Figure S12.

The negative binding free energy indicates spontaneous assembly, while positive binding free energy suggests a trend toward dissociation.

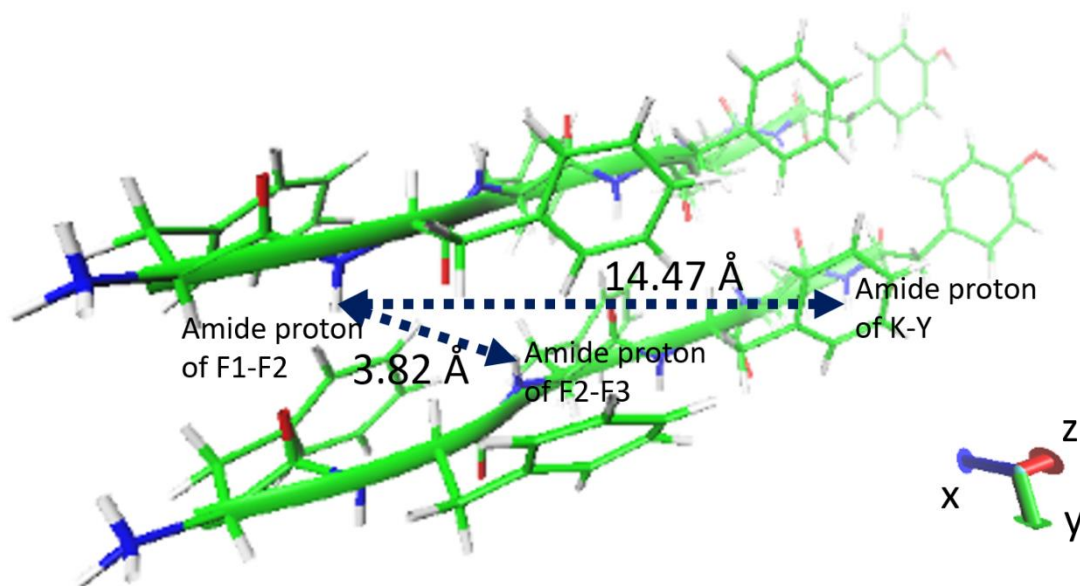


**Figure S13** Relative distance of the MD results of amide protons between F1-F2 and F2-F3, between F1-F2 and K-Y, respectively, within the parallel  $\beta$ -sheet plane. The green strips represent short peptide F<sub>4</sub>KY.

**Notes:** The relative distance is 3.82 nm between the amide proton of F1-F2 and the amide proton of F2-F3, and 14.47 nm between the amide proton of F1-F2 and the amide proton of K-Y, respectively, verifying the NOESY results to confirm the parallel conformation in the  $\beta$ -sheet (Figure 1g).

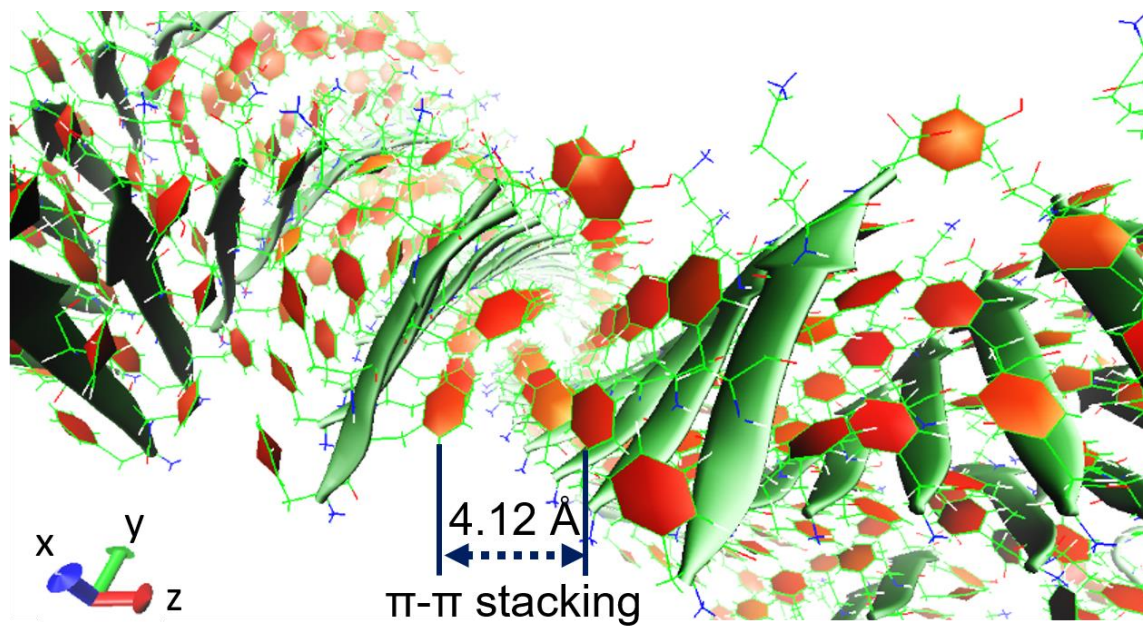


**Figure S14** MD results showing the  $\pi$ - $\pi$  stacking in the L-HFs self-assembly of F<sub>4</sub>KY. The green strips represent short peptide F<sub>4</sub>KY. The red hexagon represents the benzene ring.

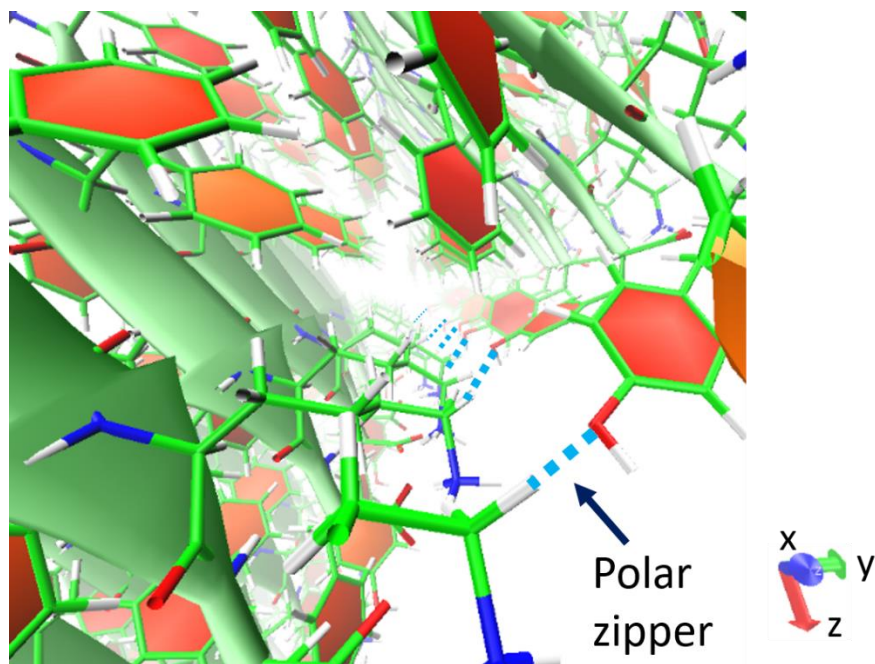


**Figure S15** MD results showing the polar zipper in the L-HFs self-assembly of F<sub>4</sub>KY.

**Notes:** The polar zipper originally proposed by Perutz is formed between neighboring  $\beta$ -strands of poly-glutamine via their sidechain hydrogen bonding and helps to stabilize the sheet. Here we demonstrate the formation of polar zippers based on the side chain of lysine and tyrosine between neighboring parallel  $\beta$ -sheets rather than between  $\beta$ -strands within a  $\beta$ -sheet, which in turn intermesh the parallel  $\beta$ -sheets into left-handed helical fibrils.

## 16. Furin-instructed L-HFs self-assembly of F<sub>4</sub>KY

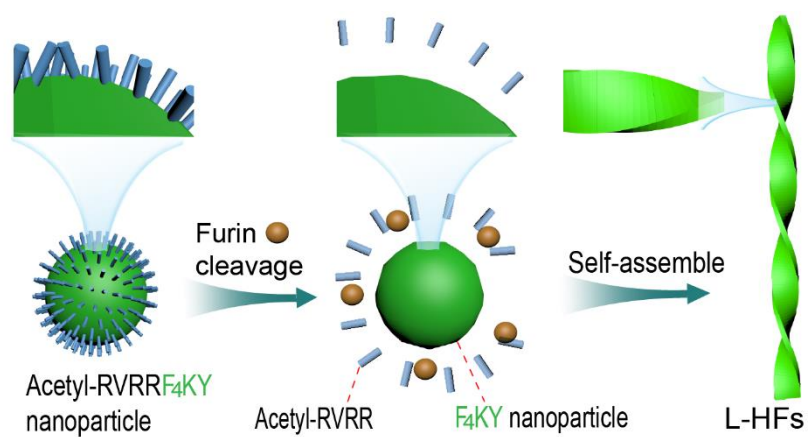


**Figure S16** Schematic illustration of the furin cleavage and L-HFs transformation process of acetyl-RVRRF<sub>4</sub>KY nanoparticles.



Acetyl-RVRRF<sub>4</sub>KY

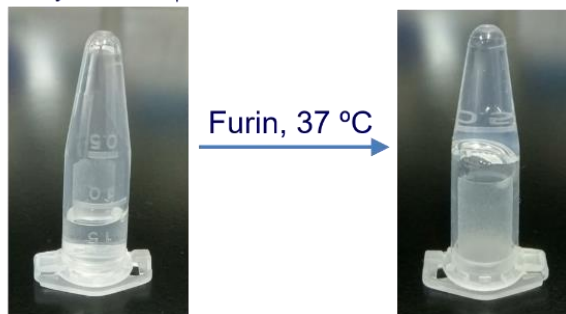


**Figure S17** Photographs showing the furin-catalyzed cleavage of acetyl-RVRRF<sub>4</sub>KY and L-HFs self-assembly of F<sub>4</sub>KY. After cleavage, the liquid in the Eppendorf tube gradually forms a gel. Experiments were repeated three times.



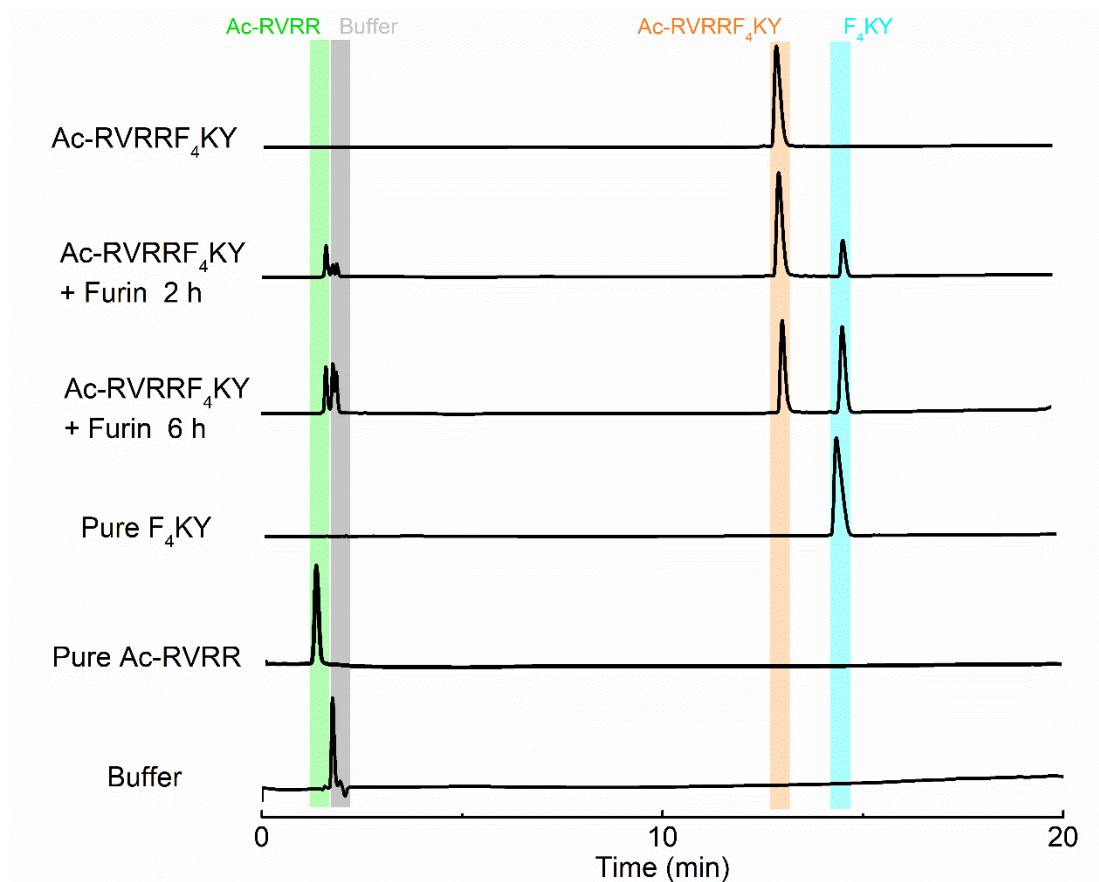


**Figure S18** HPLC results of the furin cleavage products of Ac-RVRRF<sub>4</sub>KY. Precursors Ac-RVRRF<sub>4</sub>KY (0.5 mL, 1 mg/mL) and furin (5 U) were dissolved in the 10 mM HEPES and 1 mM CaCl<sub>2</sub> buffer at 37 °C. Detection wavelength, 214 nm (SPD-20A UV/Vis Detector, SHIMADZU); Flow rate: 1 mL/min (LC-20AT Liquid chromatograph, SHIMADZU); Injection volume, 5 µL; Column, SHIMADZU Inertsil ODS-SP 4.6 µm\*150 mm\*5 µm, Column temperature, 25 °C; Buffer A, 0.1% trifluoroacetate in 100% water; Buffer B, 0.1% trifluoroacetate in 100% acetonitrile; 0.01 min, pump B 10%; 5 min, pump B 20%; 20 min, pump B 80%.

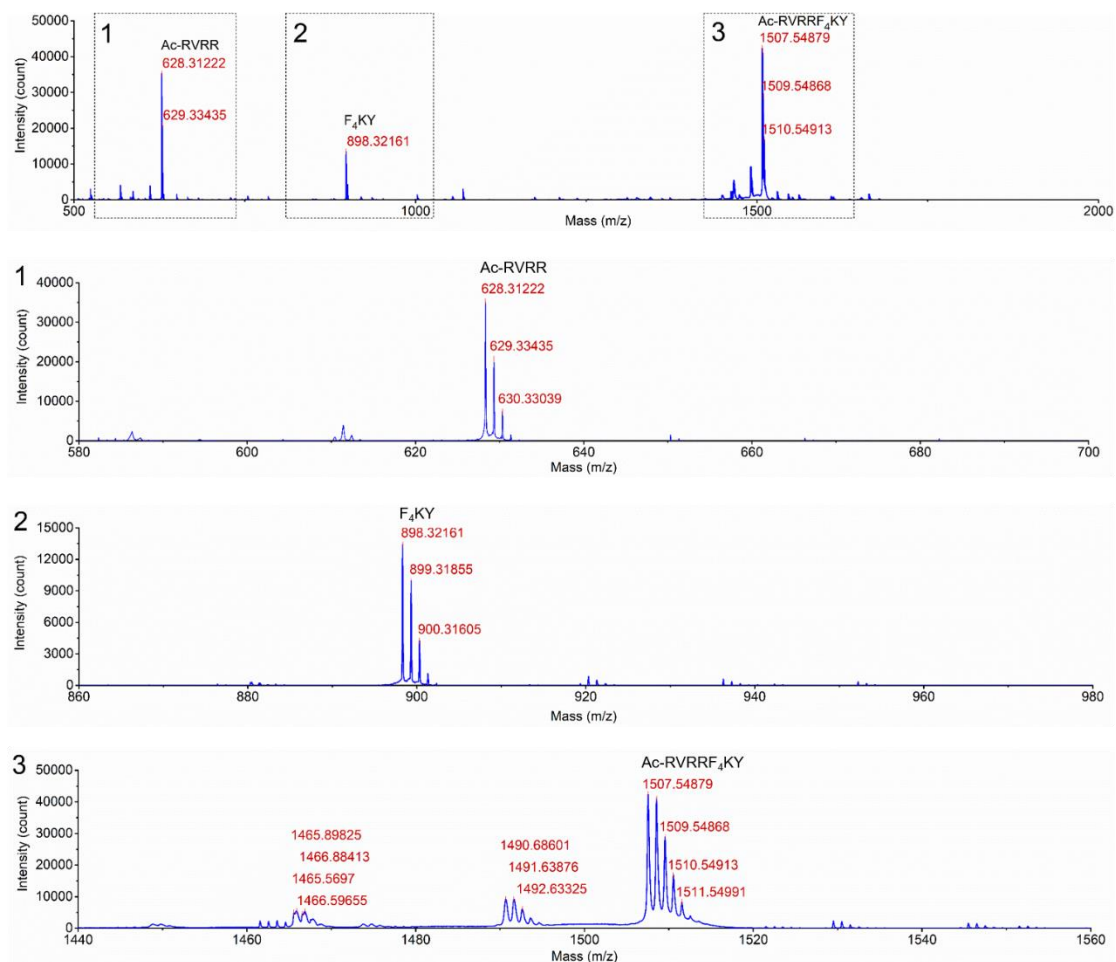


**Figure S19** MALDI-TOF mass spectra of Ac-RVRRF<sub>4</sub>KY solution after 6 h furin cleavage. Precursors Ac-RVRRF<sub>4</sub>KY (0.5 mL, 1 mg/mL) and furin (5 U) were dissolved in the 10 mM HEPES and 1 mM CaCl<sub>2</sub> buffer at 37 °C.  $\alpha$ -Cyano-4-hydroxycinnamic acid (HCCA) was used as the matrix.

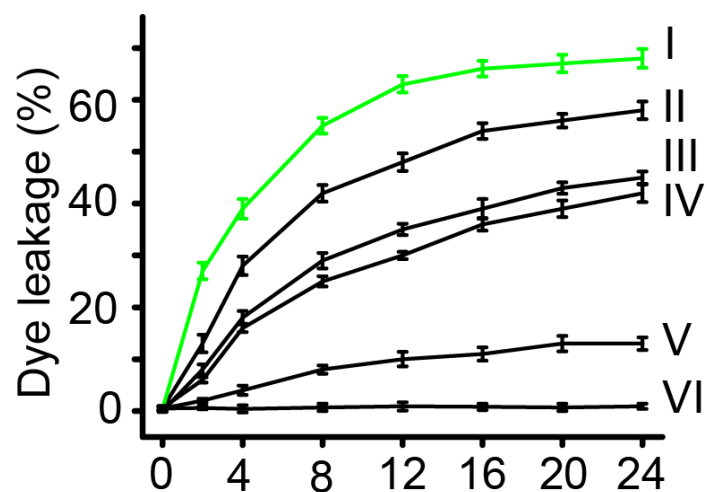


**Figure S20** The membrane disruption ability of furin-instructed L-HFs self-assembly of F<sub>4</sub>KY and its analogues inside MLV, monitored using encapsulated calcein as the indicator (excitation, 490 nm; emission, 515 nm). Data represent mean from three independent experiments, and error bars are the standard deviation. The legend for curves I to VI: I, Acetyl-RVRRF<sub>4</sub>KY + furin; II, Acetyl-RVRRF<sub>5</sub>KY + furin; III, Acetyl-RVRRF<sub>4</sub>K<sup>DY</sup> + furin; IV, Acetyl-RVRRF<sub>3</sub>KY + furin; V, Acetyl-RVRRF<sub>4</sub><sup>DY</sup>KY + furin; VI, PBS buffer without peptide and furin.

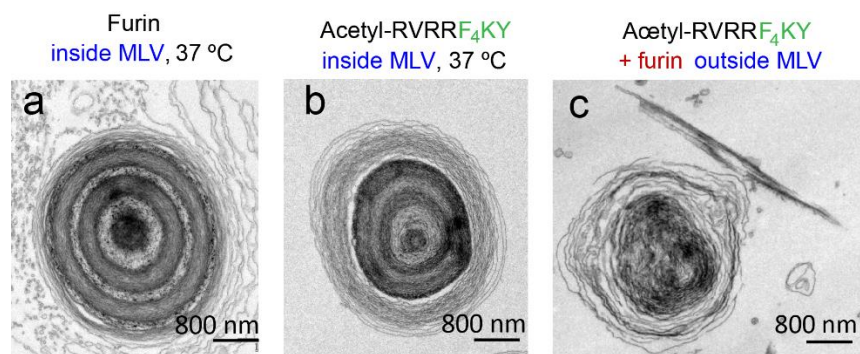


**Figure S21** TEM images of MLV without in situ self-assembly. (a) and (b) are TEM images of MLV with only furin and Ac-RVRRF<sub>4</sub>KY, respectively. c, TEM images of MLV after cleavage of Ac-RVRRF<sub>4</sub>KY by furin outside MLV.

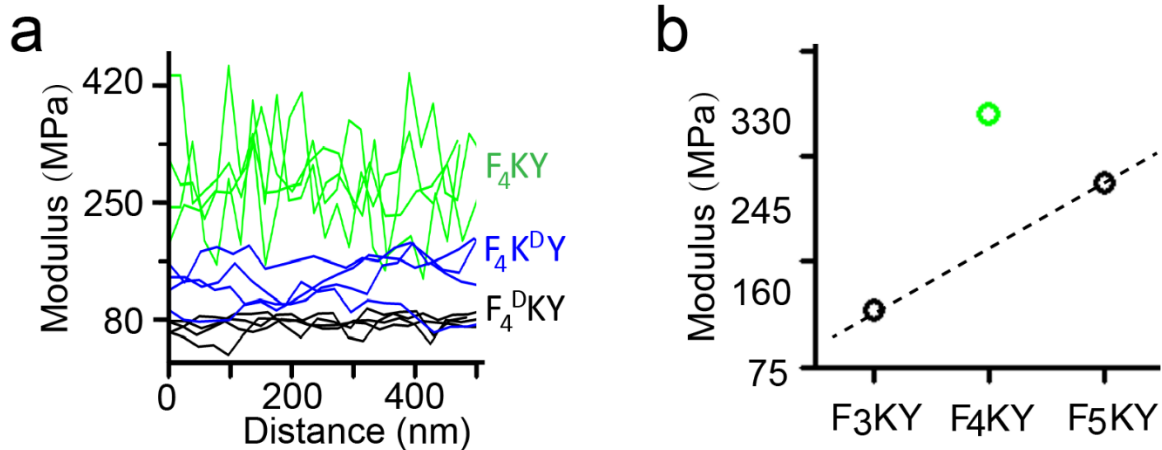


**Figure S22** The Young's modulus of L-HFs of F<sub>4</sub>KY and its analogues. **a**, Profile analysis of the Young's modulus map of the self-assemblies of F<sub>4</sub>KY, F<sub>4</sub>K<sup>D</sup>Y, and F<sub>4</sub><sup>D</sup>KY. **b**, Average Young's modulus of the self-assemblies of F<sub>3</sub>KY, F<sub>4</sub>KY, and F<sub>5</sub>KY, respectively.

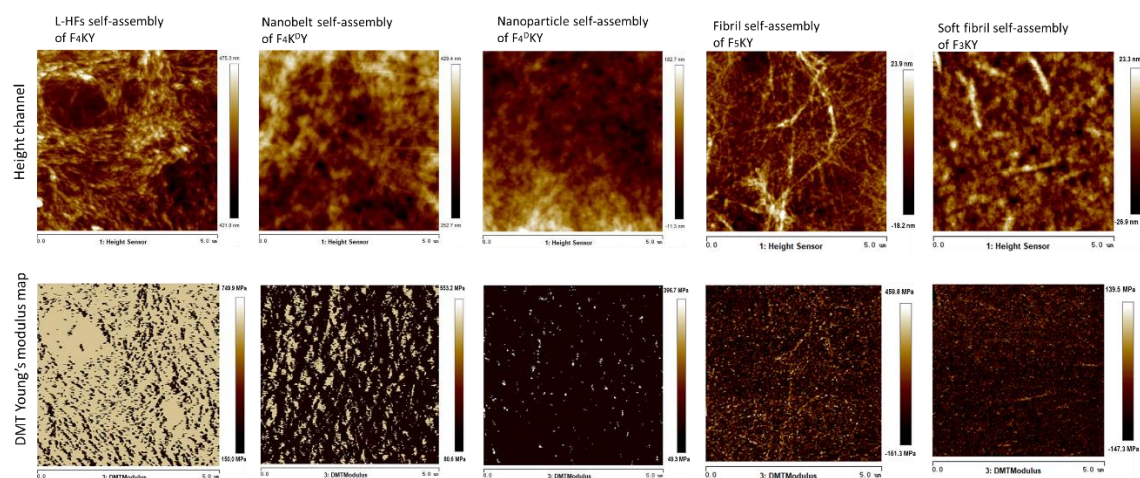


**Figure S23** The modulus test map of L-HFs self-assembly of F4KY and its analogues. The first line is the AFM height channel visualizing the surface of the stacked self-assemblies. The second line shows the corresponding Derjaguin–Mueller–Toporov (DMT) Young's modulus map.

## **17 MD simulation of the interaction between L-HFs self-assembly of F<sub>4</sub>KY and membrane**

The effect of L-HFs penetration on MLV was further investigated by the MD simulation with the Amber18 package<sup>4</sup>. With the increment of interaction time, the L-HFs self-assembly gradually bent in the membrane, and a solvent channel formed along with the bent fibril (Figure S24). At 10 ns, a distinct solvent channel along the interior bending side of the L-HFs with the thickness of 0.9 nm was generated (Figure S24); at 100 ns, the L-HFs bent at an angle about 110 degrees, and the 2.2 nm thick channel formed at the bending point (Figure S24); at 500 ns, the L-HFs further bent to an angle close to 90 degrees, and the thickness of the channel reached 3.6 nm (Figure S24). The positive correlation between the bending of the L-HFs self-assembly and the development of the solvent channel suggests that the shape transformation (bending) of the L-HFs induces the channel formation (Figures S25–S26), which might be ascribed to the mechanical tension from shape transformation of the L-HFs<sup>10</sup>. The formation of the channel may be the major event of the L-HFs associated with membrane disruption. As a result, the channels on the membrane may induce a disturbance of water and ion balance and subsequent cause the dysfunction of the living bio-system<sup>11-12</sup>.



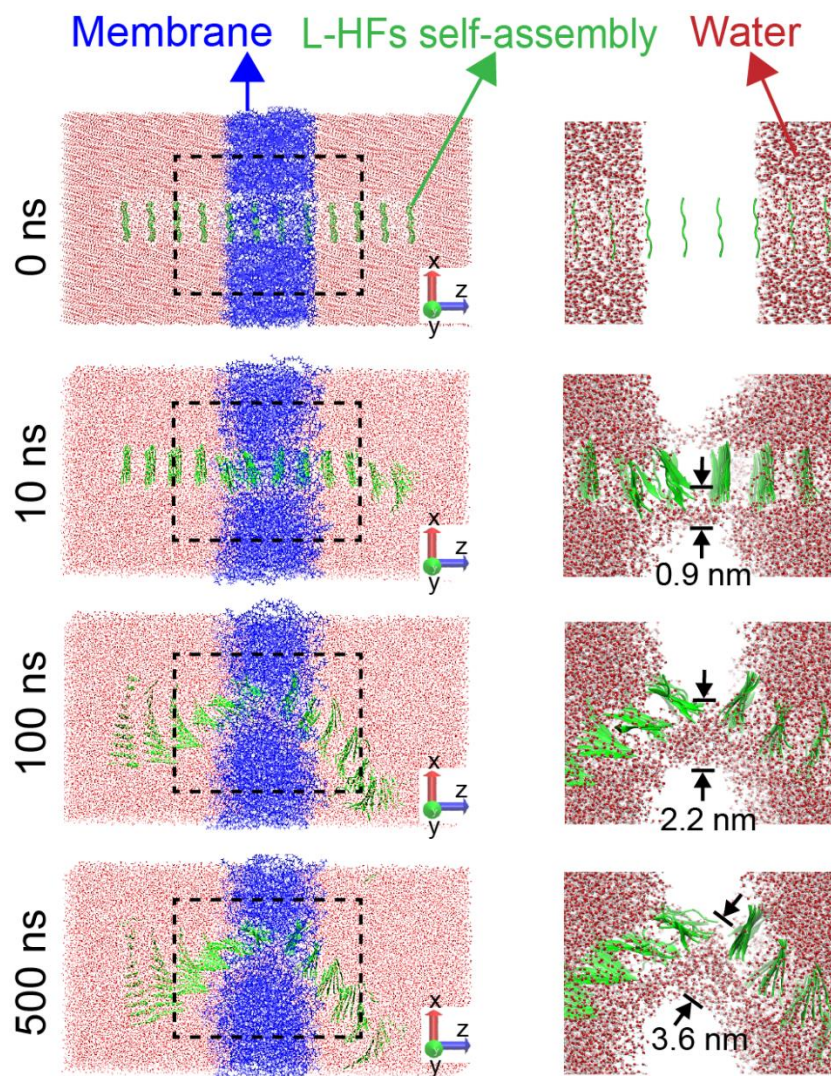


**Figure S24** The MD simulation showing the biomembrane penetration process by L-HFs self-assembly of F<sub>4</sub>KY. A giant water channel (3.5 nm) was generated after the membrane was penetrated at 500 ns. The black dotted boxes are magnified on the right with the membrane presented as white color for better visual effect of the formation of the water channel.



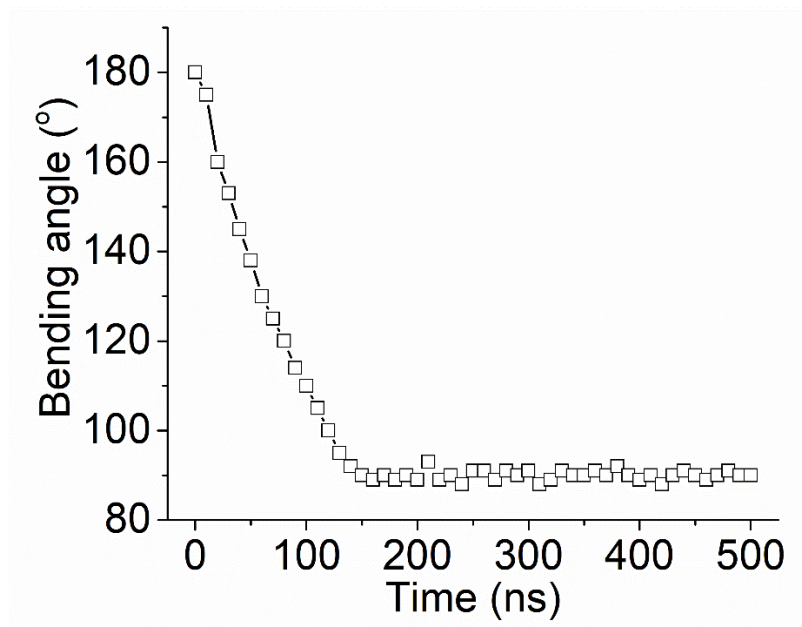


**Figure S25** MD results showing the change of bending angle of the L-HFs self-assembly of F<sub>4</sub>KY with the increasing of the interaction time of the L-HFs self-assembly of F<sub>4</sub>KY with the membrane.

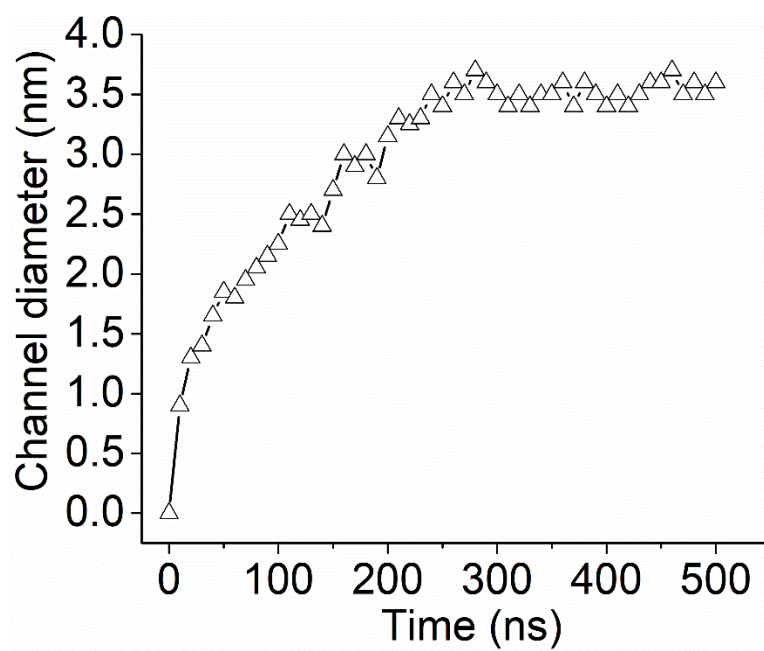


**Figure S26** MD results showing the change of the channel diameter inside the POPC bilayers membrane with the increasing of the interaction time of the L-HFs self-assembly of F<sub>4</sub>KY with the membrane.

## **18. TfR, C<sub>6</sub>, and furin-instructed L-HFs self-assembly of F<sub>4</sub>KY in the Golgi of cancer cells**

### **18.1 Precursor design for cell uptake and targeting of the Golgi of cancer cells**

In our previous work<sup>13</sup>, the multivalent effect of cysteines on nanomaterials presents the potential for the Golgi targeting. In this work, we synthesized a series of polycysteine peptides C<sub>*n*</sub>R with *n* from 4 to 8 to screen the suitable number of cysteines that can present the maximum effect of cell uptake and Golgi targeting of cancer cells. Arginine (R) is attached to C-terminal of the polycysteine peptide to improve the water solubility of polycysteine. Fluorescein (FAM) is linked on the N-terminal of C<sub>*n*</sub>R to track their location. The cell viability results show that peptides C<sub>*n*</sub>R with the number of cysteine from 4 to 6 have low cell toxicity (Figure S28). The high toxicity of peptides with 7 and 8 cysteines may be attributed to the low water solubility. Amongst peptide with 4–6 cysteines, 6 cysteines present excellent Golgi-specific targeting performance (Figure S29), thus is used in this study.

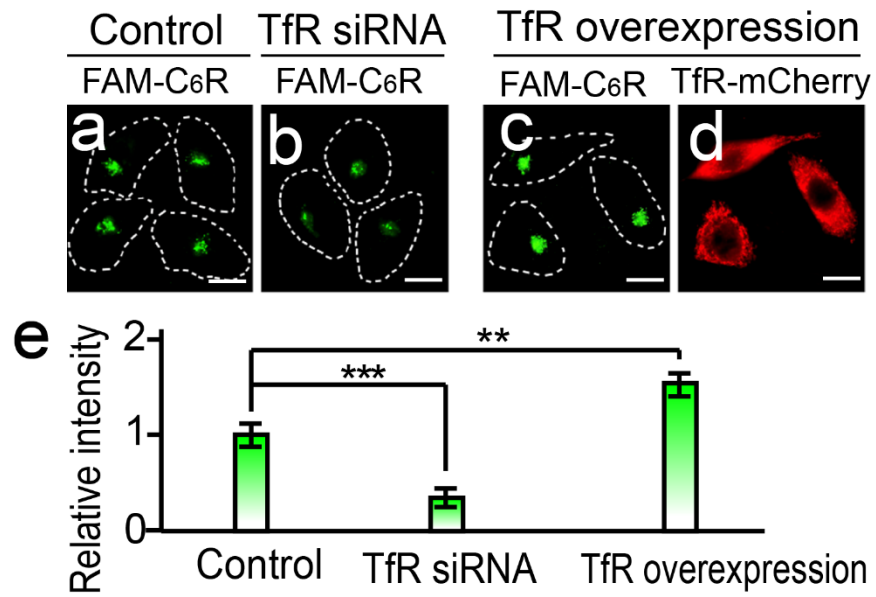


**Figure S27** TfR recognition by C<sub>6</sub>. **a–c**, The fluorescence images of FAM-C<sub>6</sub>R in MCF-7 cells with knockdown or overexpression of TfR. Scale bar, 10  $\mu$ m. **d**, The fluorescence image of TfR-mCherry. **e**, Quantification of FAM-C<sub>6</sub>R uptake with knockdown or overexpression of TfR. \*\* means  $p < 0.01$ ; \*\*\* means  $p < 0.001$ .

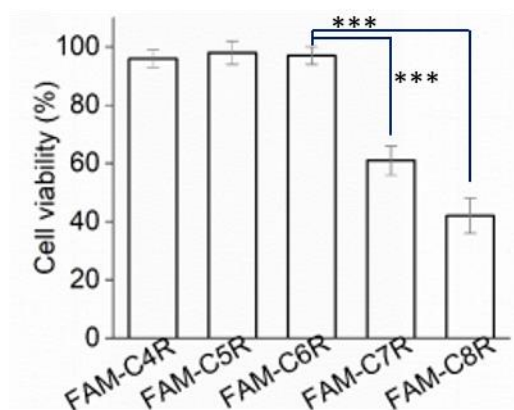


**Figure S28** Cell viability of FAM-C<sub>4</sub>R, FAM-C<sub>5</sub>R, FAM-C<sub>6</sub>R, FAM-C<sub>7</sub>R, and FAM-C<sub>8</sub>R after 24 h of incubation with MCF-7 cells. Data are presented as mean  $\pm$  s.d. (n=3). \*\* means  $p < 0.01$ .

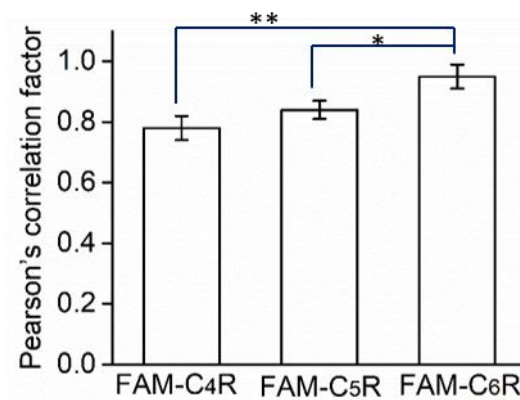


**Figure S29** Pearson's correlation factor of fluorescent polycysteine and Bodipy ceramide in MCF-7 cells after 4 h of incubation, calculated by Image-Pro Plus 6.0. Data are presented as mean  $\pm$  s.d. ( $n=3$ ). \* means  $p < 0.05$ ; \*\* means  $p < 0.01$ .

## 18.2 Cancer cell Golgi apparatus targeting ability of C<sub>6</sub>R

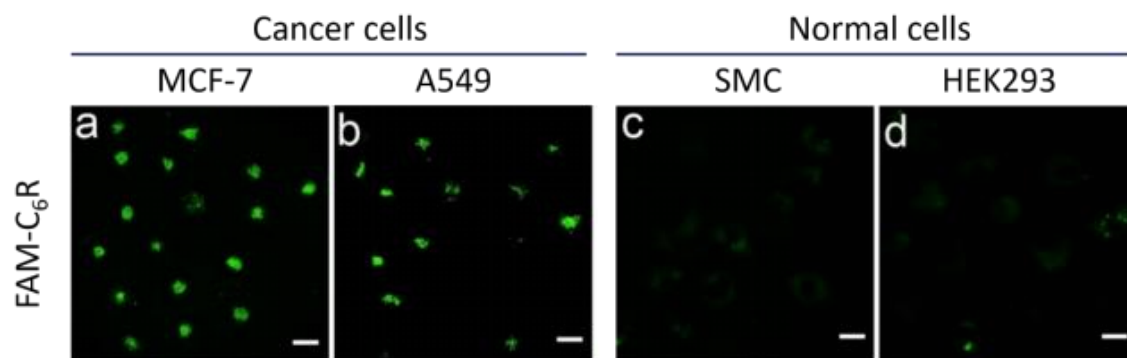


**Figure S30** Fluorescence images of FAM-C<sub>6</sub>R (20  $\mu$ M) in incubation with cancer cells. Scale bar, 10  $\mu$ M. The results clearly show that C<sub>6</sub>R can specifically target cancer cells. Experiments were repeated three times.

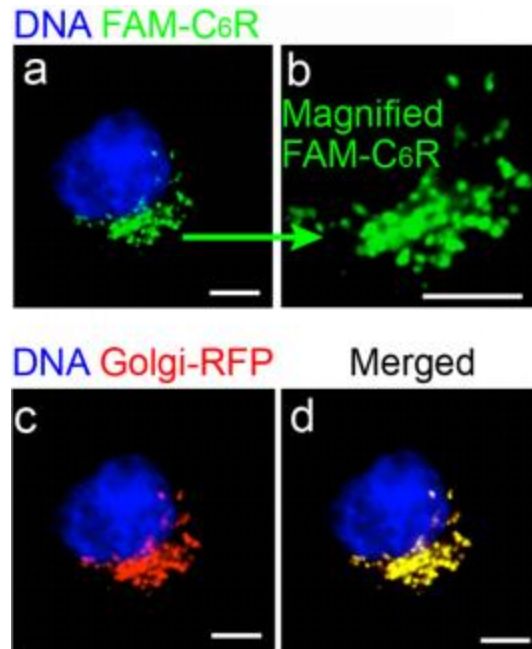


**Figure S31** Co-localization of FAM-C<sub>6</sub>R and Golgi-RFP in MCF-7 cell. **a**, Fluorescence image of FAM-C<sub>6</sub>R (green) and DNA (blue) in MCF-7 cell. **b**, Magnified fluorescence image of FAM-C<sub>6</sub>R. **c**, Fluorescence image of N-acetylgalactosaminyltransferase-RFP (Golgi-RFP, red) and DNA (blue). **d**, Merged image of a and c. Scale bar, 10  $\mu$ M. Experiments were repeated three times.

**Notes:** specific Golgi targeting ability of the C<sub>6</sub> is demonstrated by co-staining FAM-C<sub>6</sub>R with N-acetylgalactosaminyltransferase-RFP (Golgi-RFP), the red fluorescence probes for Golgi-staining. The fluorescent area of FAM-C<sub>6</sub>R matches very well with Golgi-RFP with a Pearson's correlation factor higher than 0.95, indicating that preferential accumulation of the FAM-C<sub>6</sub>R in the Golgi has occurred.



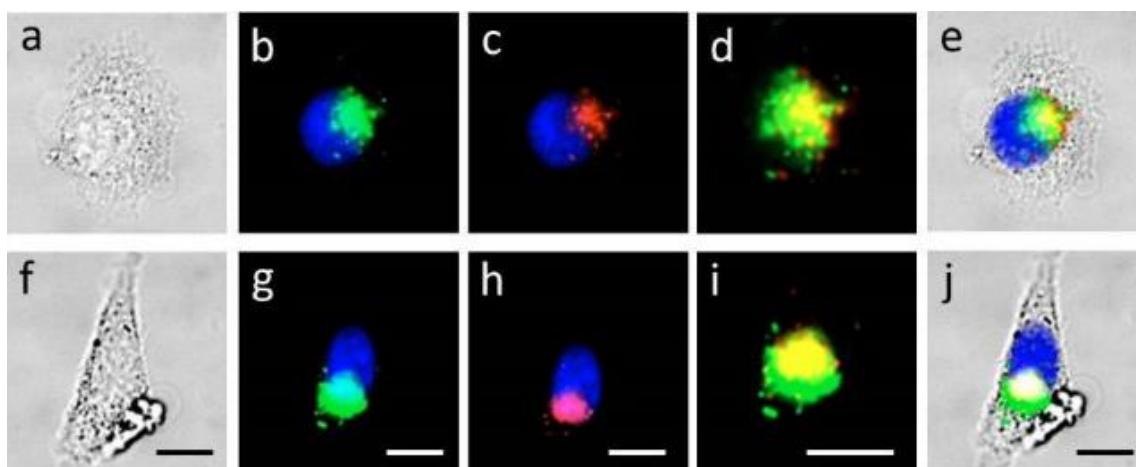


**Figure S32** Immunofluorescence image of the Golgi. a, Bright light image of MCF-7 cell. b, Fluorescence image of DNA (blue, stained by hoechst 33258) and FAM-C<sub>6</sub>R (green). c, Immunofluorescence image of DNA and *cis*-Golgi. The primary antibody was anti-GM130 and the secondary antibody was Rabbit IgG-H&L (Cy3®). d, e, Merged images of fluorescence and bright field images. f, Bright light image of MCF-7 cell. g, Fluorescence image of DNA (blue, stained by hoechst 33258) and FAM-C<sub>6</sub>R (green). h, Immunofluorescence image of DNA and *trans*-Golgi. The primary antibody was anti-TGN46 and the secondary antibody was Rabbit IgG-H&L (Cy3®). i, j, Merged images of fluorescence and bright field images. Scale bar, 10 μm. Experiments were repeated three times.

**Notes:** Immunofluorescence results suggest that the FAM-C<sub>6</sub>R can stain both the *cis*-Golgi and *trans*-Golgi.

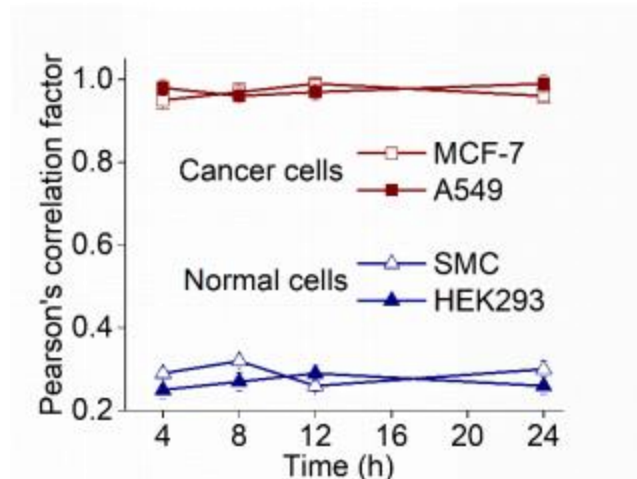


**Figure S33** Pearson's correlation factor between FAM-C<sub>6</sub>R and Bodipy ceramide in different cell lines as a function of incubation time, calculated by Image-Pro Plus 6.0. Data are presented as mean  $\pm$  s.d. ( $n=3$ ).

**Notes:** The analysis of Pearson's correlation factor indicates that accumulation of the FAM-C<sub>6</sub>R occurs preferentially in the Golgi of cancer cells.

### 18.3 The L-HFs self-assembly of F<sub>4</sub>KY in the Golgi of cancer cells

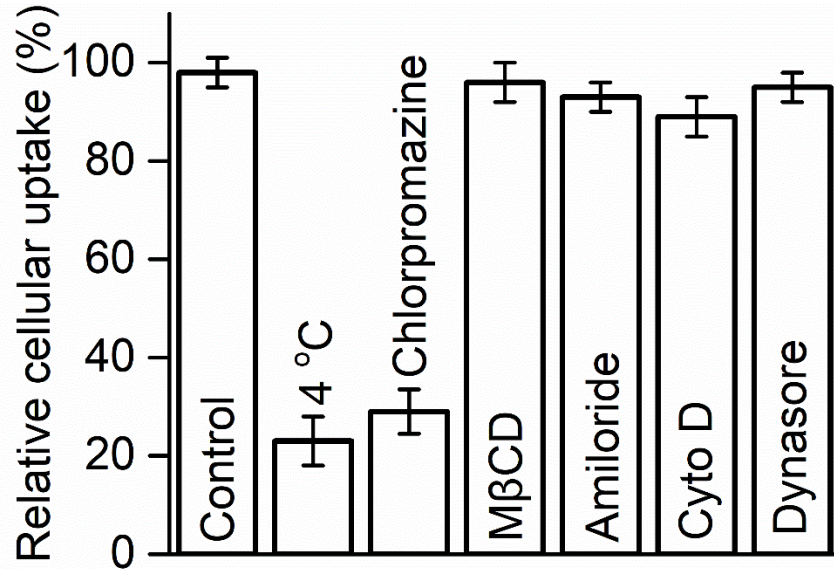


**Figure S34** The influence of different inhibitors on the cellular uptake of C<sub>6</sub>RVRRF<sub>4</sub>KY. Error bars represent standard deviations from five replicate experiments. Low temperature (4 °C) can inhibit the activity of ATPase and reduce the production of cell energy. MβCD: Methyl-β-cyclodextran; Cyto D: Cytochalasin D. Chlorpromazine is the inhibitor of clathrin; Cyto D can reduce the amount of cholesterol on the membrane and inhibit caveolae-mediated endocytosis; Amiloride inhibits pinocytosis; Cyto D is the inhibitor of actin polymerization; Dynasore can inhibit the GTPase activity of dynamin. Data are presented as mean ± s.d. (*n* = 3).

**Notes:** The results indicate that the uptake of C<sub>6</sub>RVRRF<sub>4</sub>KY is an energy-dependent process mediated by TfR and subsequent clathrin-mediated endocytosis pathway.

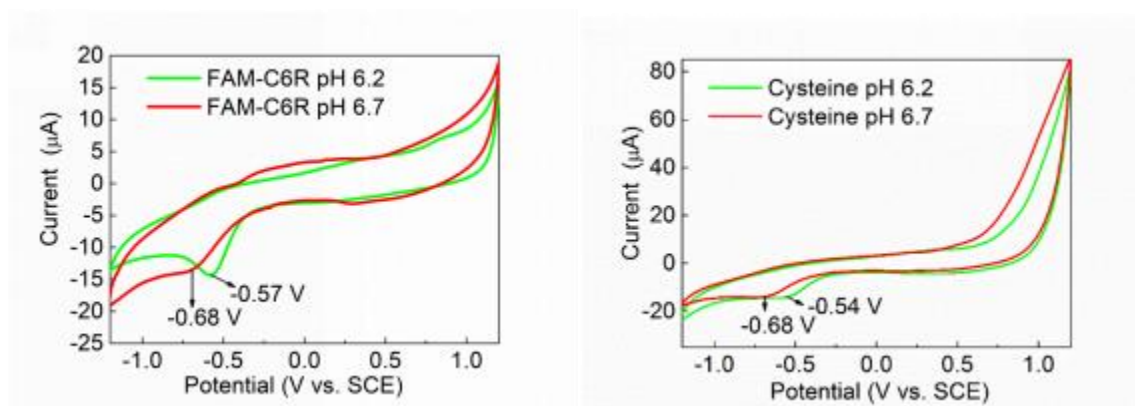


**Figure S35** Cyclic voltammetric curves of FAM-C<sub>6</sub>R (left) and cysteine (right) at pH 6.2 and 6.7. Experiments were repeated three times.

**Notes:** The results indicate that the Golgi targeting carrier C<sub>6</sub>R is easily oxidized at the pH similar to that in the Golgi, which can be attributed to the oxidation of cysteine residues.

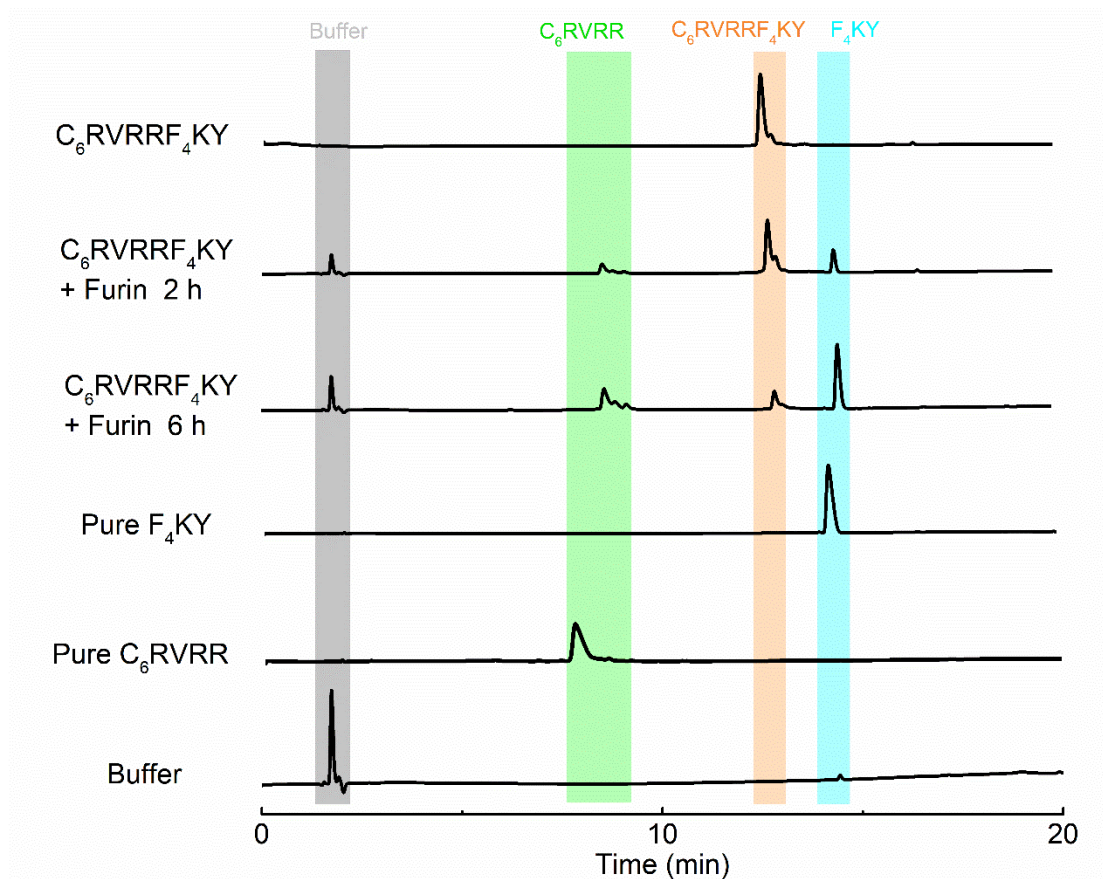


**Figure S36** HPLC results of the furin cleavage products of C<sub>6</sub>RVRRF<sub>4</sub>KY. Precursors C<sub>6</sub>RVRRF<sub>4</sub>KY (0.5 mL, 1 mg/mL) and furin (5 U) were dissolved in the 10 mM HEPES and 1 mM CaCl<sub>2</sub> buffer at 37 °C. Detection wavelength, 214 nm (SPD-20A UV/Vis Detector, SHIMADZU); Flow rate: 1 mL/min (LC-20AT Liquid chromatograph, SHIMADZU); Injection volume, 5 µL; Column, SHIMADZU Inertsil ODS-SP 4.6 µm\*150 mm\*5 µm, Column temperature, 25 °C; Buffer A, 0.1% trifluoroacetate in 100% water; Buffer B, 0.1% trifluoroacetate in 100% acetonitrile; 0.01 min, pump B 10%; 5 min, pump B 20%; 20 min, pump B 80%.

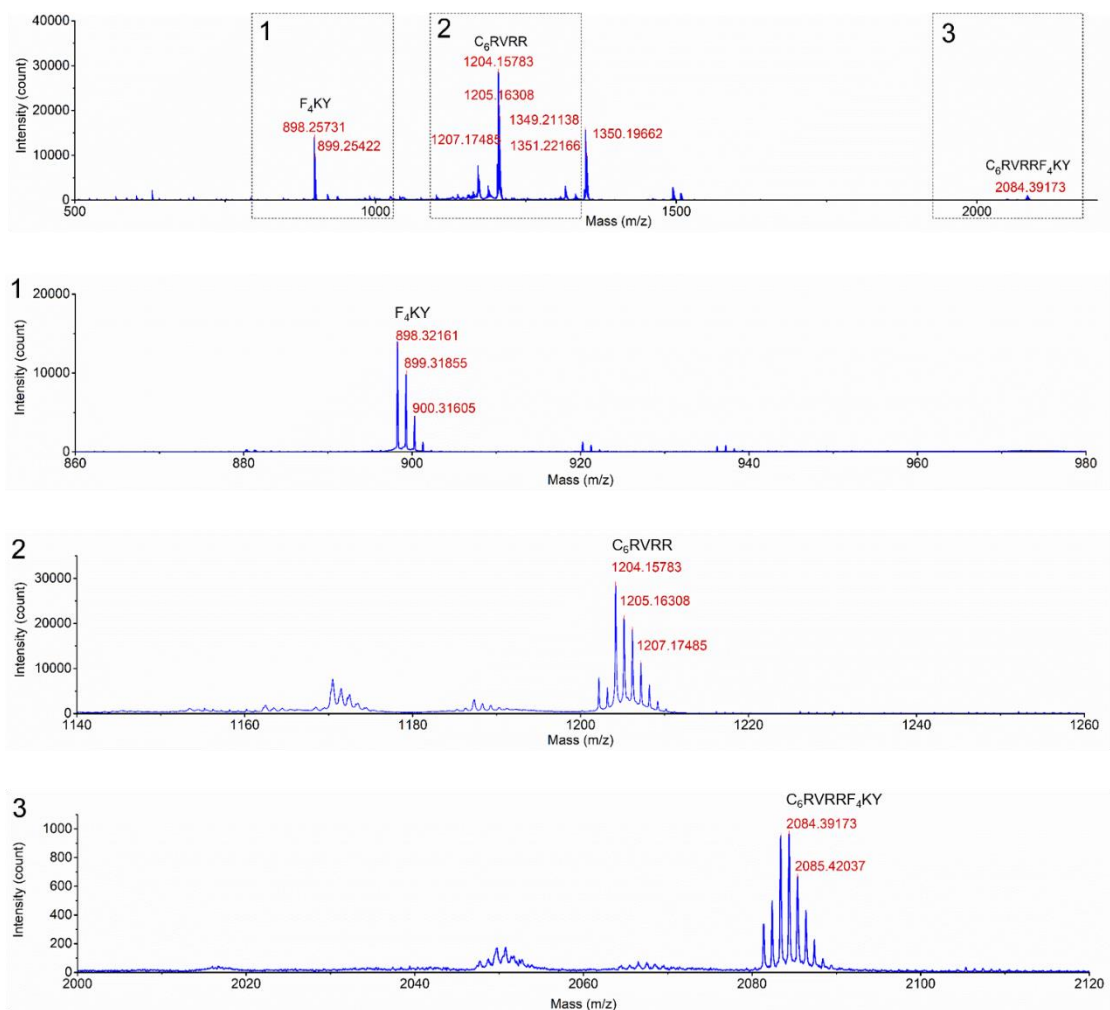


**Figure S37** The MALDI-TOF mass spectra of C<sub>6</sub>RVRRF<sub>4</sub>KY solution after 6 h furin cleavage. Precursors C<sub>6</sub>RVRRF<sub>4</sub>KY (0.5 mL, 1 mg/mL) and furin (5 U) were dissolved in the 10 mM HEPES and 1 mM CaCl<sub>2</sub> buffer at 37 °C. α-Cyano-4-hydroxycinnamic acid (HCCA) was used as the matrix.

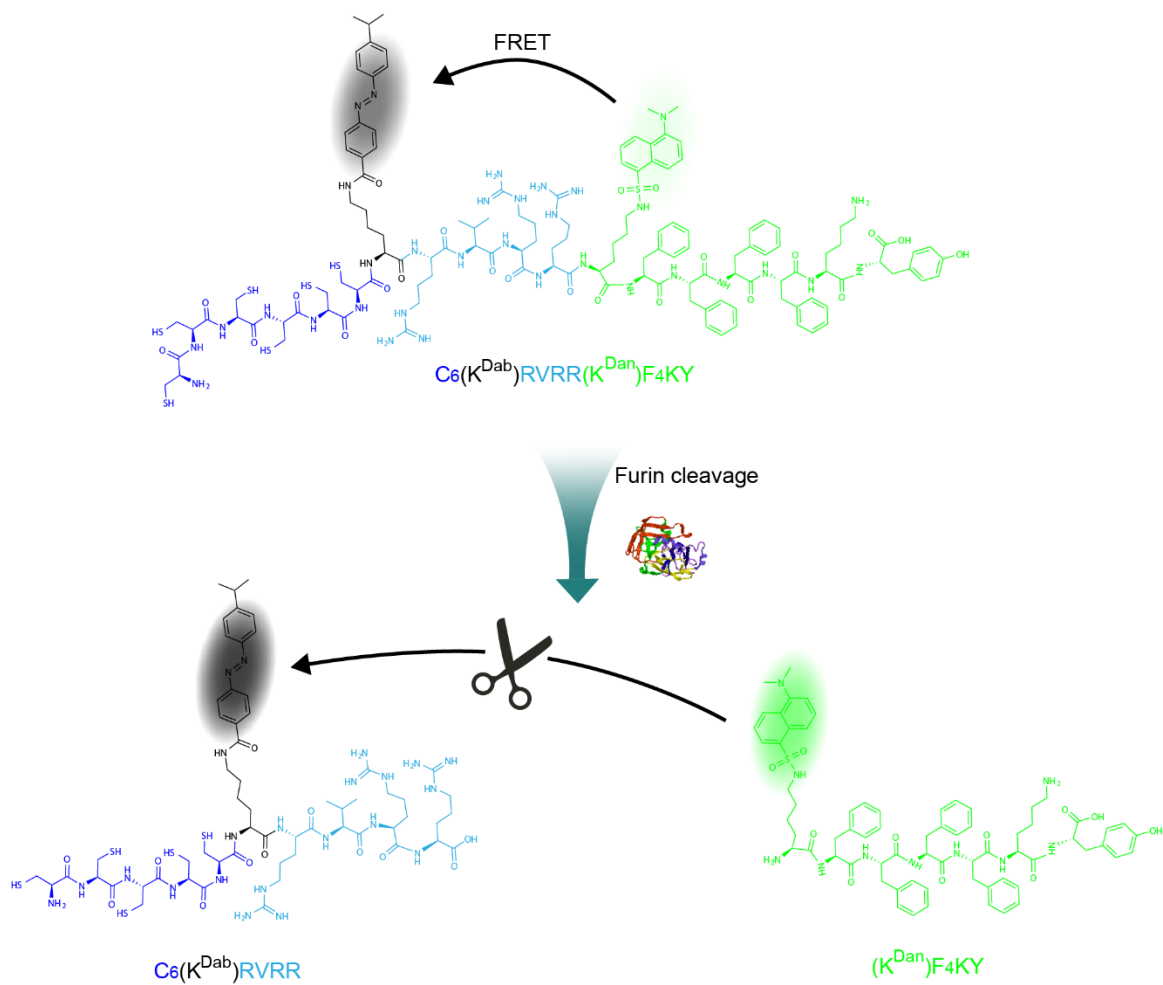


**Figure S38** Illustration of the structure of  $C_6(K^{Dab})RVRR(K^{Dan})F_4KY$  and its cleavage products.



**Figure S39** Optical and fluorescence images of  $\text{C}_6(\text{K}^{\text{Dab}})\text{RVRR}(\text{K}^{\text{Dan}})\text{F}_4\text{KY}$  before and after introducing furin.



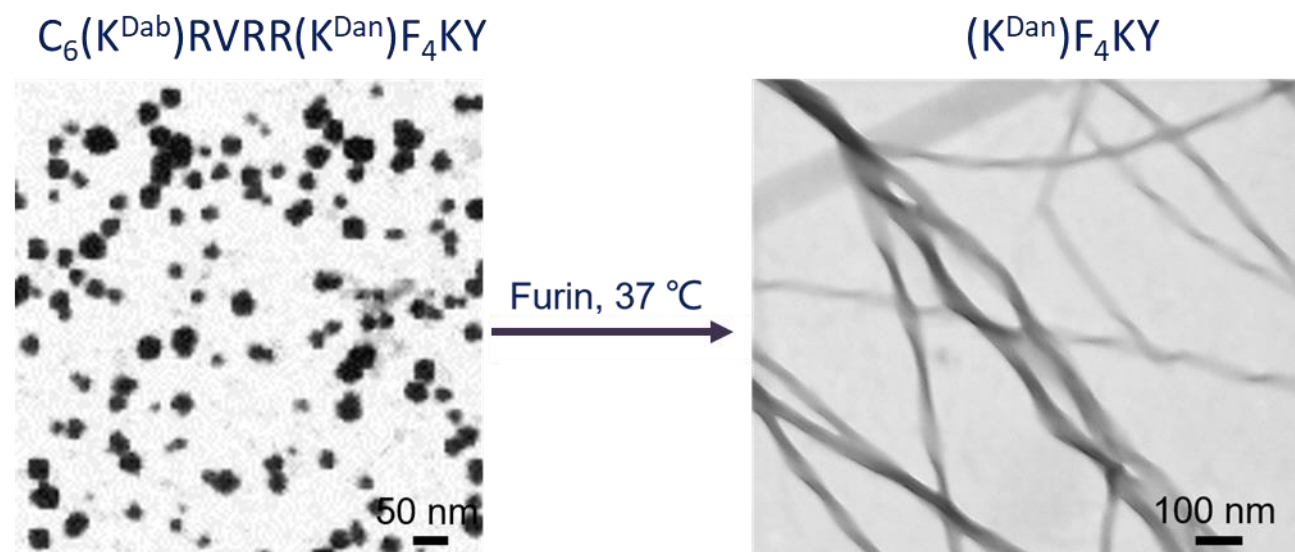


**Figure S40** Furin-instructed cleavage of  $C_6(K^{Dab})RVRR(K^{Dan})F_4KY$  ( $31 \pm 16$  nm) and self-assembly of fluorescent  $(K^{Dan})F_4KY$ . Experiments were repeated three times.

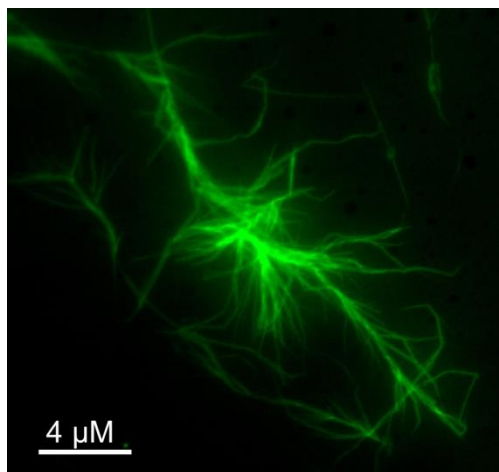


**Figure S41** The fluorescence image of the self-assembly of fluorescent (K<sup>Dan</sup>)F4KY after furin-instructed cleavage of C<sub>6</sub>(K<sup>Dab</sup>)RVRR(K<sup>Dan</sup>)F4KY. Experiments were repeated three times.

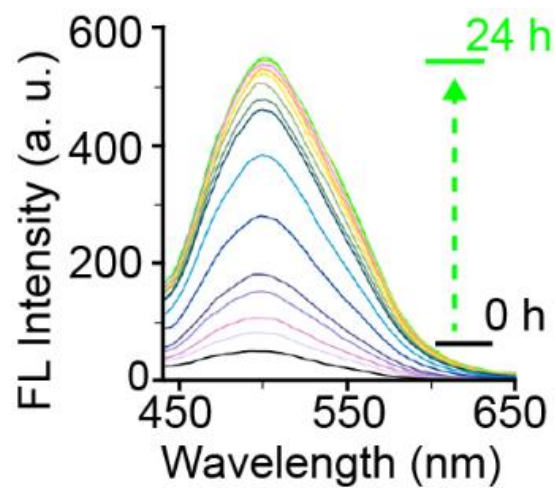


**Figure S42** Furin-instructed cleavage of  $C_6(K^{Dab})RVRR(K^{Dan})F_4KY$  monitored by fluorescence spectra at different time after introducing furin. Experiments were repeated three times.

**Notes:** The result indicates that the amount of  $F_4KY$  increases with the increment of the time of furin-instructed cleavage.

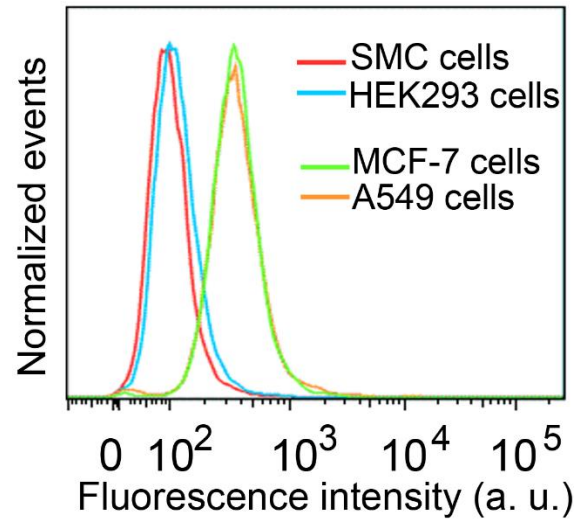


**Figure S43** Flow cytometry histograms of cancer and normal cell lines that were incubated with  $C_6(K^{Dab})RVRR(K^{Dan})F_4KY$ .

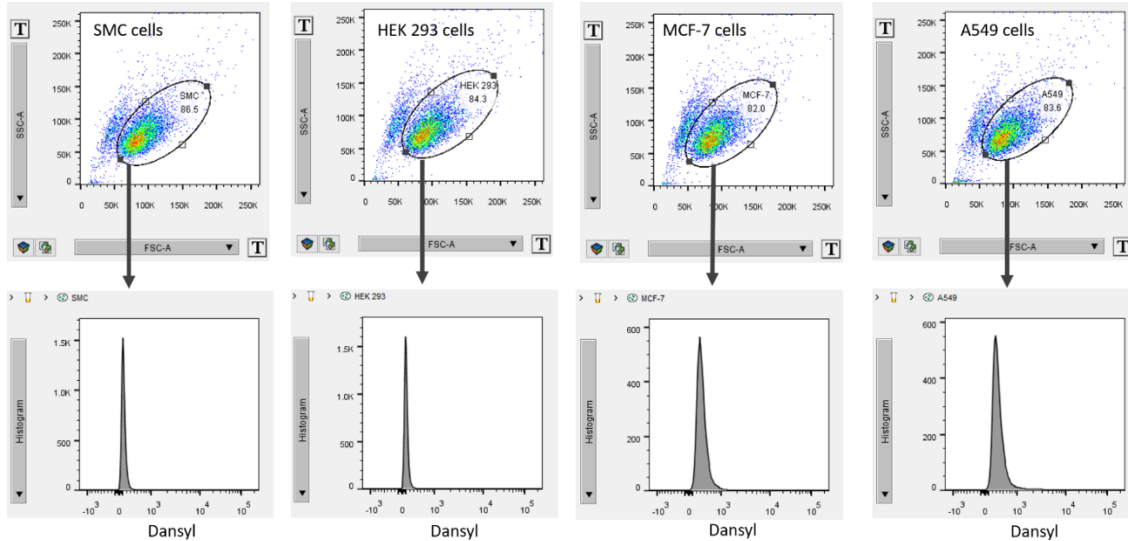


**Figure S44** Flow cytometry gating strategy used in the Figure S43. After 4 h incubation of the cancer cells with  $C_6(K^{Dab})RVRR(K^{Dan})F_4KY$  nanoparticles, strong fluorescence was observed in the cancer cell lines by fluorescence cytometry, indicating massive TfR-mediated cellular uptake and the formation of furin cleavage product  $(K^{Dan})F_4KY$  in the Golgi apparatus of cancer cells. In contrast, the normal cell lines showed negligible fluorescence. Experiments were repeated three times.

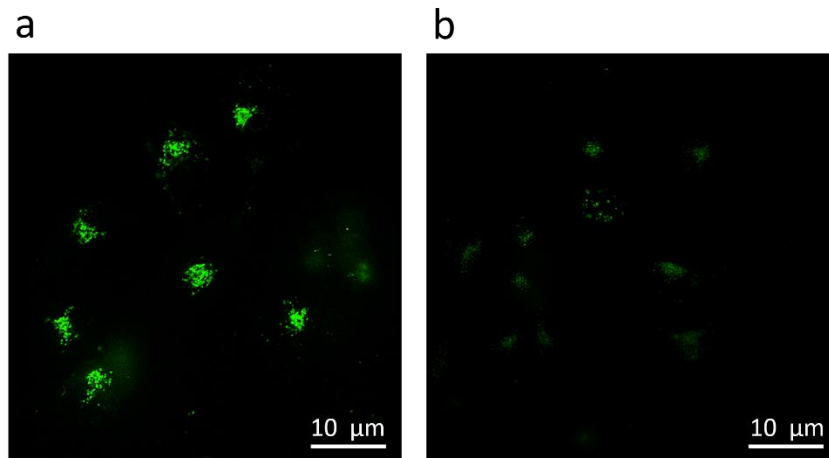


**Figure S45** The influence of furin inhibitor on peptide cleavage. (a) Fluorescence image of  $C_6(K^{Dab})RVRR(K^{Dan})F_4KY$  (50  $\mu M$ ) without furin inhibitor after 4 h incubation in MCF-7 cells. (b) Fluorescence image of  $C_6(K^{Dab})RVRR(K^{Dan})F_4KY$  (50  $\mu M$ ) with furin inhibitor, Hexa-D-arginine amide (50  $\mu M$ ), after 4 h incubation in MCF-7 cells.

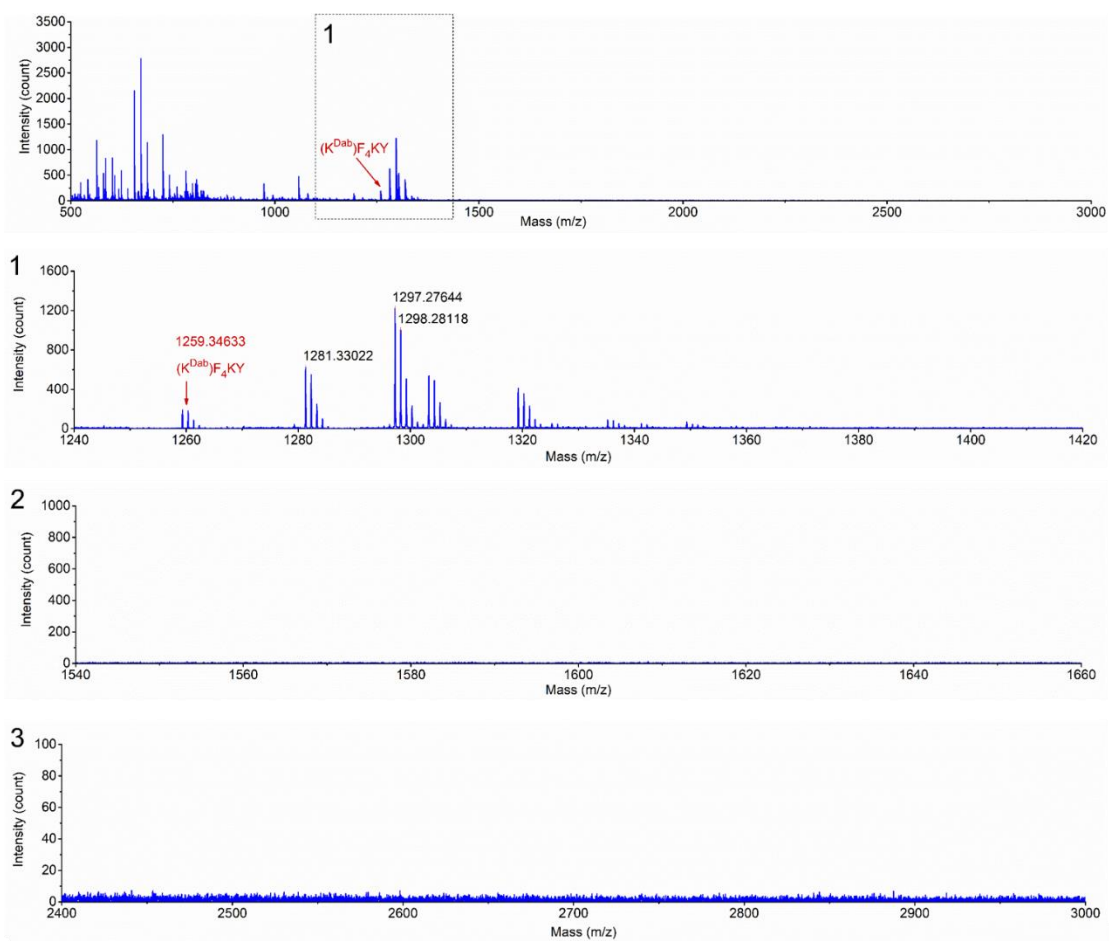


**Figure S46** The MALDI-TOF mass spectra of MCF-7 cell extract after 4 h incubation with C<sub>6</sub>(K<sup>Dab</sup>)RVRR(K<sup>Dan</sup>)F<sub>4</sub>KY (50 μM). Sample preparation process is in the Methods. α-Cyano-4-hydroxycinnamic acid (HCCA) was used as the matrix.

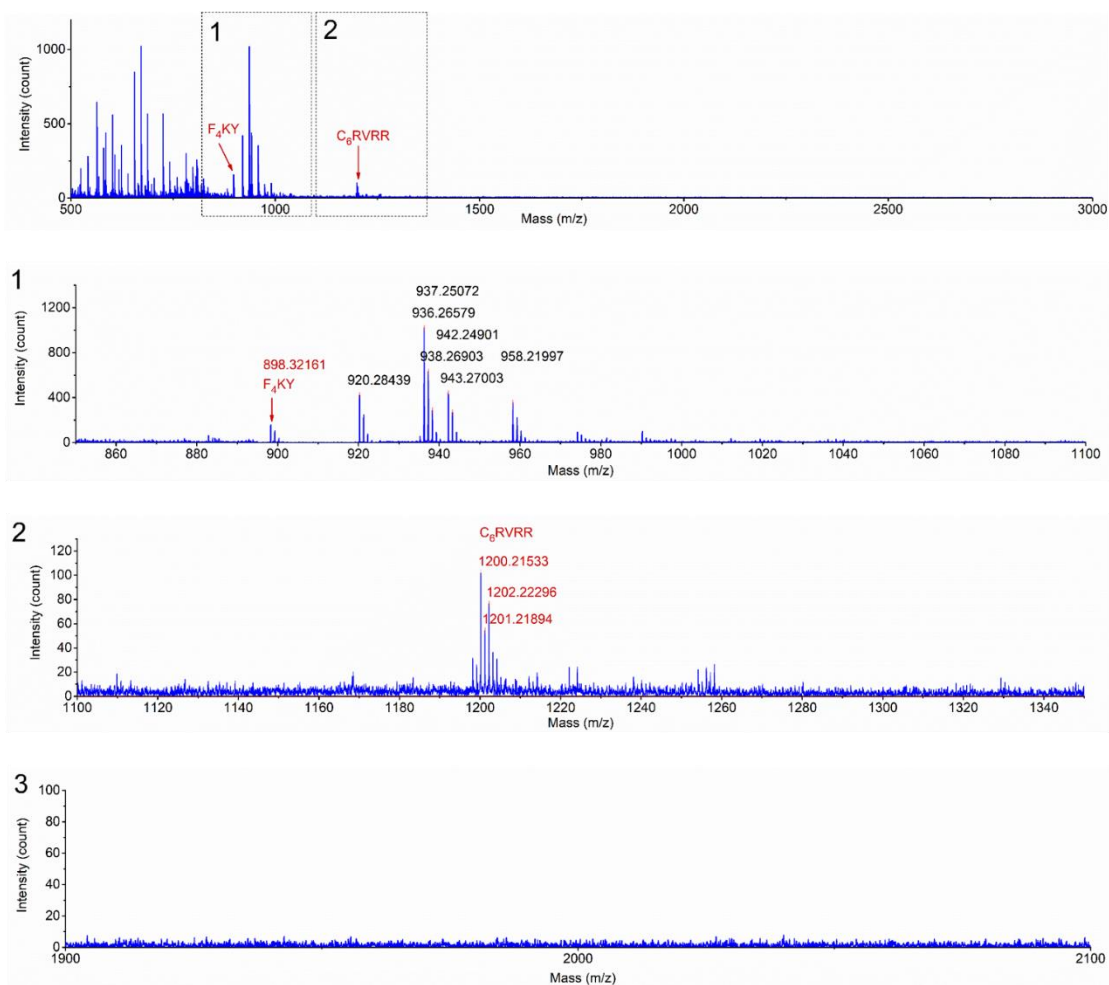


**Figure S47** The MALDI-TOF mass spectra of MCF-7 cell extract after 4 h incubation with  $C_6VRRF_4KY$  (50  $\mu M$ ). Sample preparation process is in the Methods.  $\alpha$ -Cyano-4-hydroxycinnamic acid (HCCA) was used as the matrix.



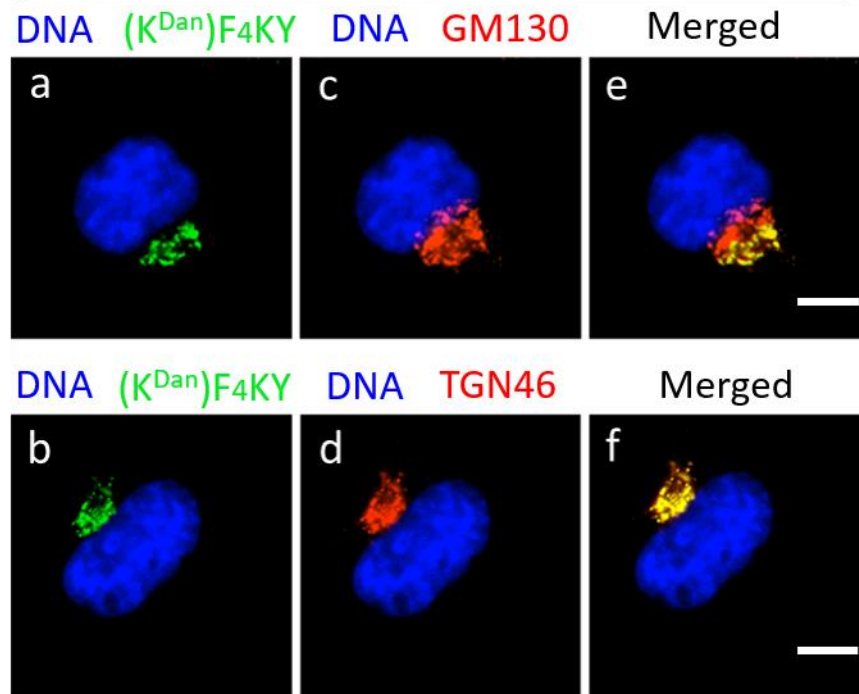


**Figure S48** Immunofluorescence image of cis-Golgi or trans-Golgi when MCF-7 cells were incubated by C<sub>6</sub>(K<sup>Dab</sup>)RVRR(K<sup>Dan</sup>)F<sub>4</sub>KY. Fluorescence image of the (K<sup>Dan</sup>)F<sub>4</sub>KY (green, a and b). The primary antibody of *cis*-Golgi was (c) anti-GM130. The primary antibody of *trans*-Golgi was (d) anti-TGN46. The secondary antibody was Rabbit IgG–H&L (Cy3). Red color is the fluorescence of Golgi RFP. Blue color is the fluorescence of DNA stained by Hoechst 33258. Scale bar, 5  $\mu$ m. Experiments were repeated three times.

**Notes:** The merged images (e and f) indicate that the F<sub>4</sub>KY is mainly assembled in the *trans*-Golgi.

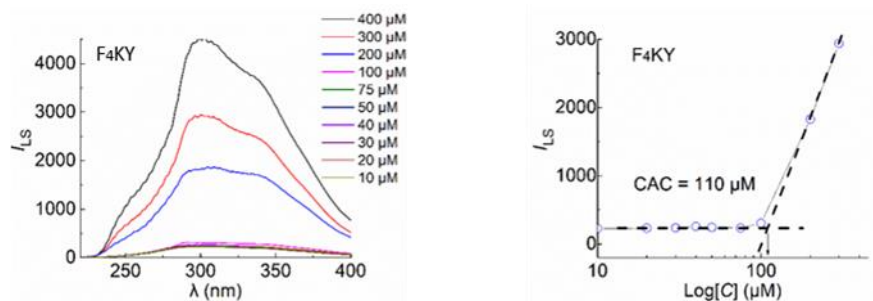


**Figure S49** Light scattering spectra of F4KY at different concentrations (left) and the relationship between scattering intensity and concentrations (right).

**Notes:** According to Pasternack *et al.* and Huang *et al.*<sup>14-15</sup>, a particle, assumed to be spherical, absorbs and scatters light depending on its size, shape and refractive index relative to the surrounding medium. When the irradiation power is fixed, light-scattering is proportional to the scattering cross section:

$$C_{\text{sca}} = (\pi r^2) \left( \frac{8}{3} \right) x^4 \left[ \frac{(m^2 - 1)}{(m^2 + 2)} \right]^2$$

where  $r$  is the radius of spherical particle;  $m = n_{\text{sph}}/n_{\text{med}}$ ;  $n_{\text{sph}}$  is the refractive index of the sphere;  $n_{\text{med}}$  is the refractive index of the surrounding medium; and  $x$  is the size parameter, equal to  $2\pi r n_{\text{med}}/\lambda$ .

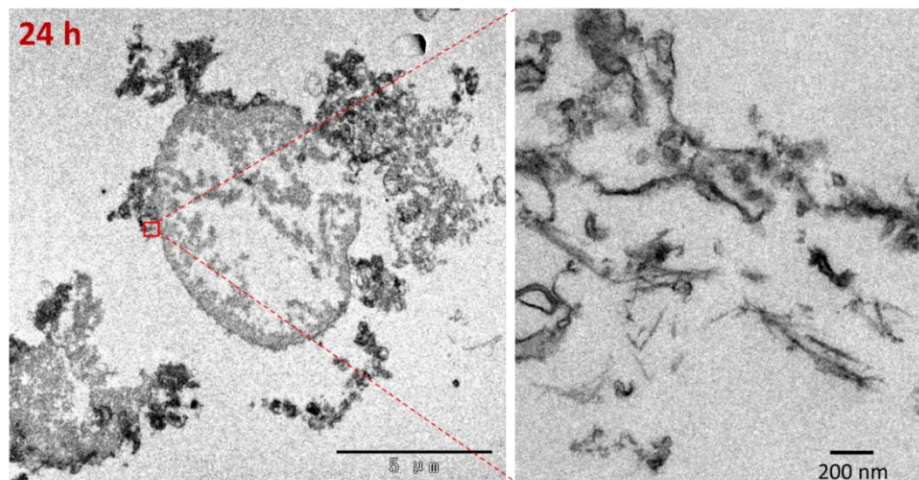


**Figure S50** TEM images of furin-instructed L-HFs self-assembly in the Golgi after 24 h incubation of C<sub>6</sub>RVRRF<sub>4</sub>KY with MCF-7 cells. Experiments were repeated three times.

**Notes:** The results indicate that the Golgi membrane gradually disappeared, and necrosis happened in MCF-7 cells after 24 h incubation of C<sub>6</sub>RVRRF<sub>4</sub>KY.

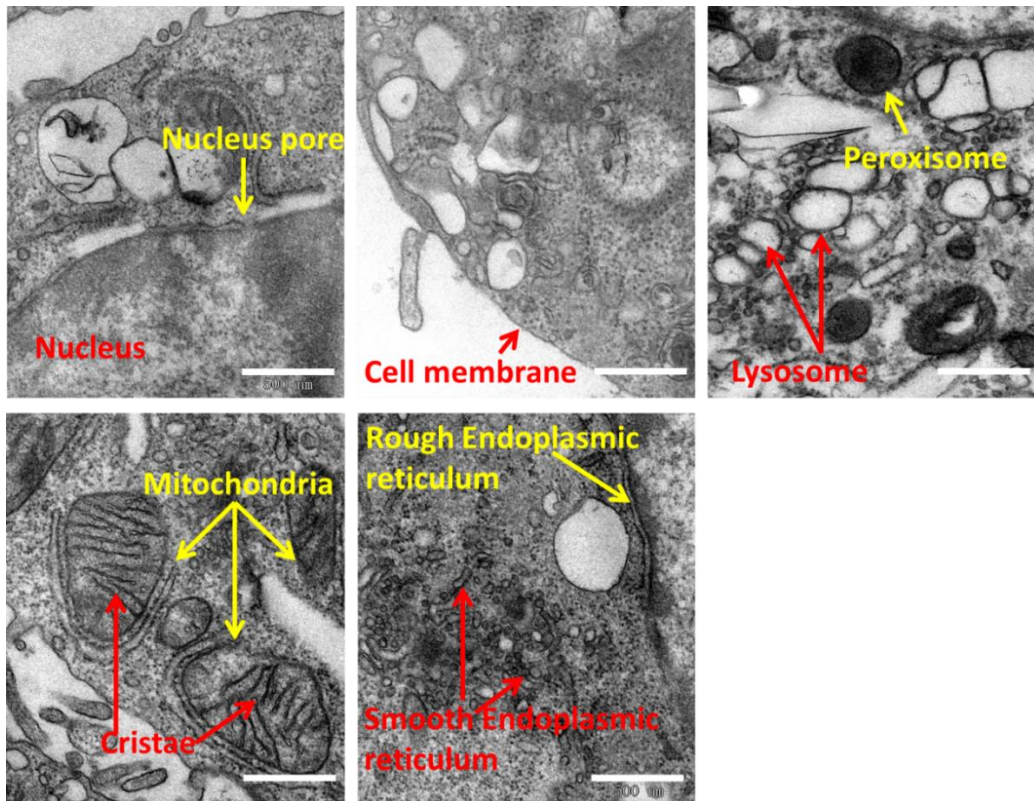


**Figure S51** TEM images the nucleus, cell membrane, lysosomes, mitochondria and endoplasmic reticulum of MCF-7 cells after 4 h of incubation with C<sub>6</sub>RVRRF<sub>4</sub>KY (50  $\mu$ M). Scale bar, 500 nm. Experiments were repeated three times.

**Notes:** No fibrillar structures or precipitates can be found in these subcellular organelles, indicating the specificity of self-assembly of peptide in the Golgi.

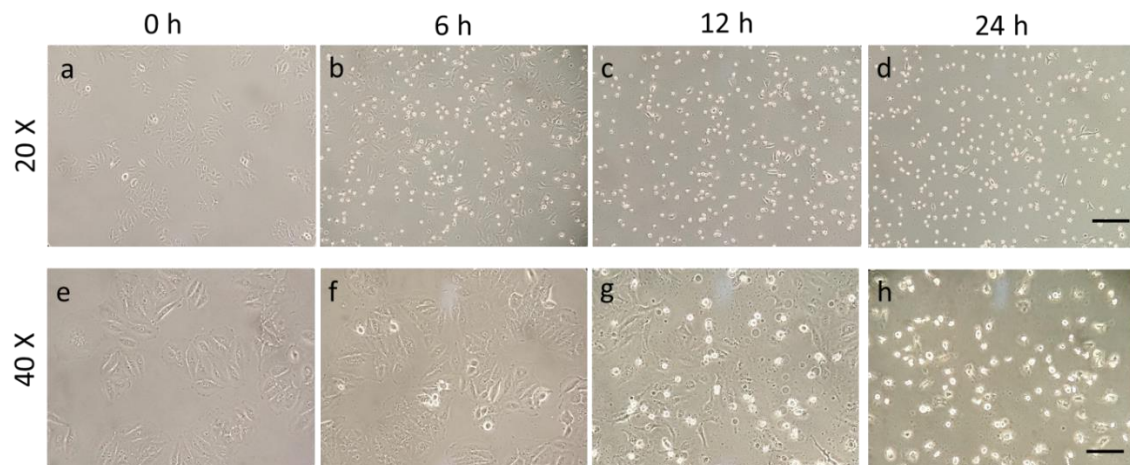


**Figure S52** Images of MCF-7 cells at different time and different magnification after incubation with C<sub>6</sub>RVRRF<sub>4</sub>KY. Scale bar, 100 μm (a–d) and 50 μm (e–h). Experiments were repeated three times.  
**Notes:** As the incubation time increased, the cancerous MCF-7 cells gradually died.

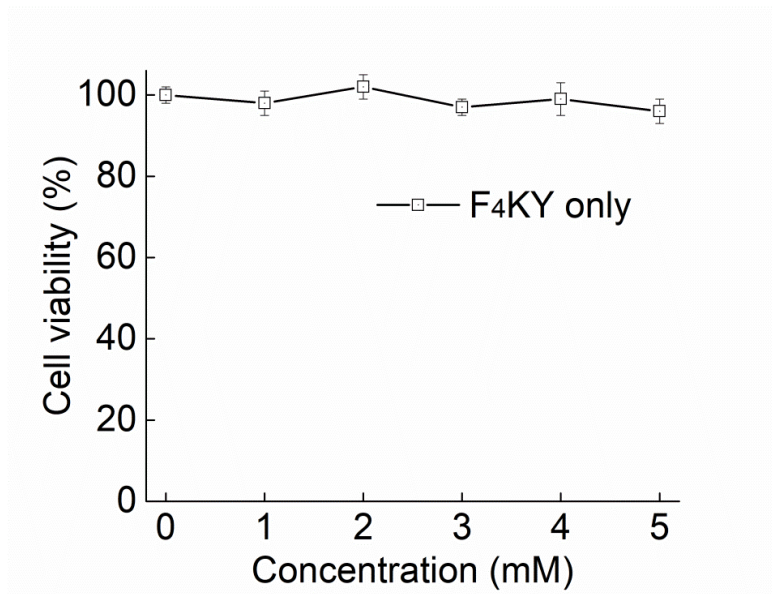


**Figure S53** The MCF-7 cells cytotoxicity data of F<sub>4</sub>KY peptide with different concentration after 24 h incubation.

**Notes:** F<sub>4</sub>KY peptide can form a gel when the concentration is higher than 3 mM. The addition of the pre-assembly L-HFs of F<sub>4</sub>KY (5 mM) into the cell culture medium did not cause toxicity to MCF-7 cell lines.

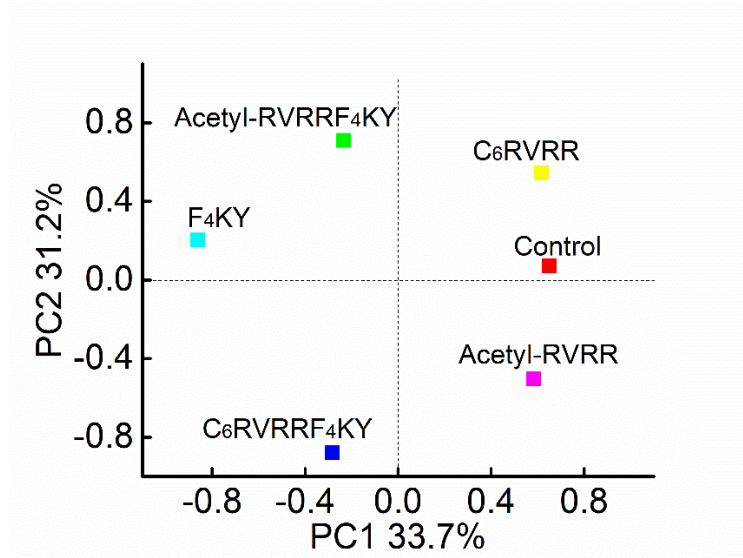


**Figure S54** Principal component analysis of the cytokine secretion with IBM SPSS Statistics 22. Experiments were repeated three times.

**Notes:** The analysis results indicate that the cytokine secretion caused by C<sub>6</sub>RVRRF<sub>4</sub>KY is different from that induced by Acetyl-RVRRF<sub>4</sub>KY, Acetyl-RVRR, C<sub>6</sub>RVRR, and F<sub>4</sub>KY.

## Appendix 1 Mass spectrometric analysis of peptides

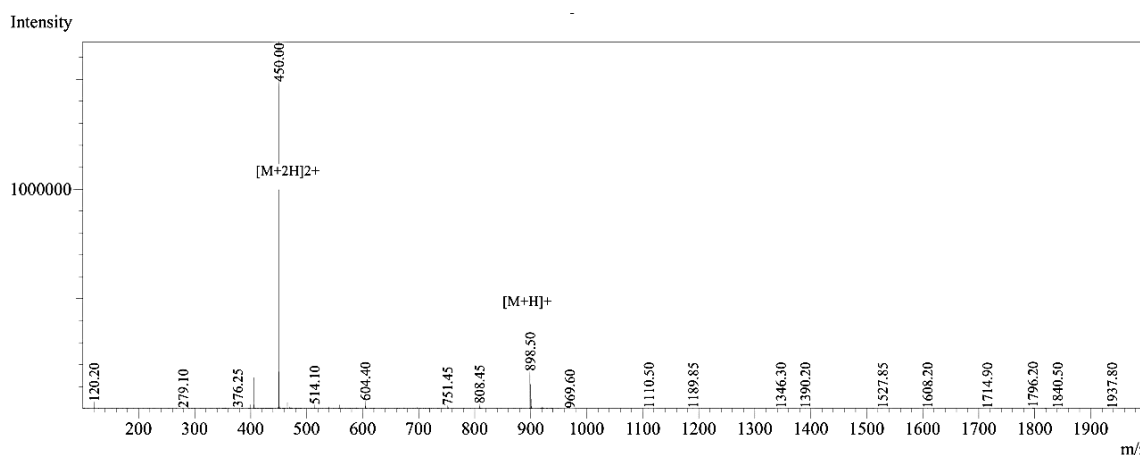


**Figure A1** Mass spectrum of F<sub>4</sub>KY. Dissolution method: 0.1 mg sample dissolved to 0.5 mL by 25% ACN and 75% H<sub>2</sub>O. Probe: ESI. Nebulizing gas flow: 1.5 L/min. CDL temperature: 250 °C. Block temperature: 200 °C. T. flow: 0.2 mL/min. B. conc: 50% H<sub>2</sub>O/50% MeOH. The results indicate the formation of F<sub>4</sub>KY.



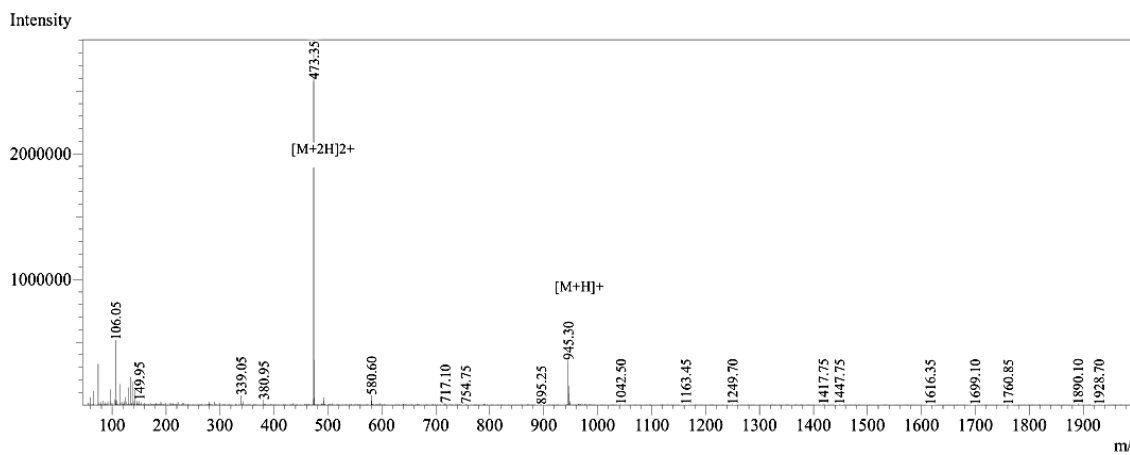


**Figure A2** Mass spectrum of FAM-C<sub>4</sub>R. Dissolution method: 0.1 mg sample dissolved to 0.5 mL by 20% ACN and 80% H<sub>2</sub>O. Probe: ESI. Nebulizing gas flow: 1.5 L/min. CDL temperature: 250 °C. Block temperature: 200 °C. T. flow: 0.2 mL/min. B. conc: 50% H<sub>2</sub>O/50% MeOH. The results indicate the formation of FAM-C<sub>4</sub>R.

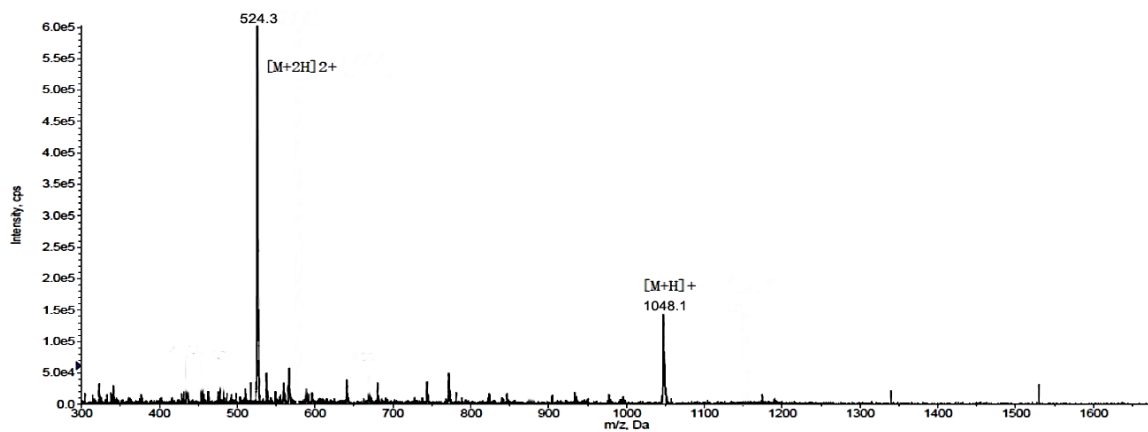


**Figure A3** Mass spectrum of FAM-C<sub>5</sub>R. Dissolution method: 0.5 mg sample dissolved to 0.5 mL by 100% H<sub>2</sub>O. Probe: ESI. Nebulizing gas flow: 1.5 L/min. CDL temperature: 250 °C. Block temperature: 200 °C. T. flow: 0.2 mL/min. B. conc: 50% H<sub>2</sub>O/50% MeOH. The results indicate the formation of FAM-C<sub>5</sub>R.

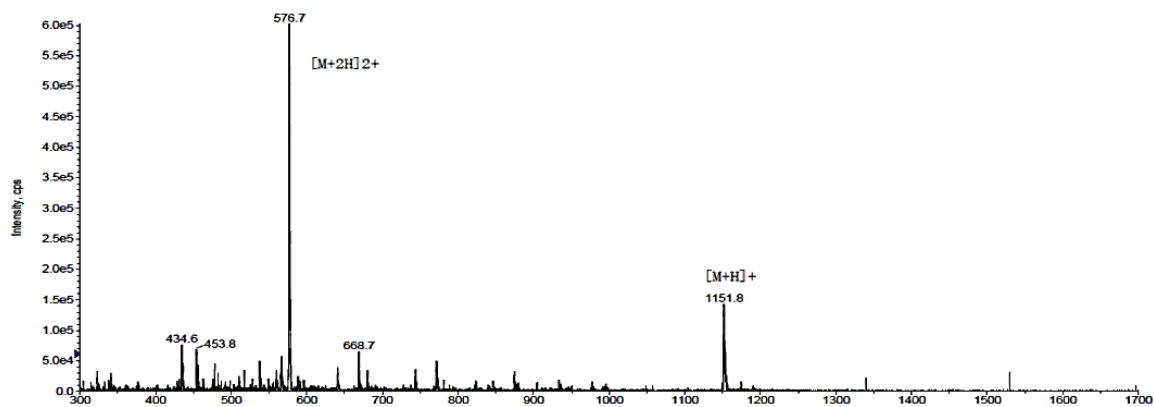


**Figure A4** Mass spectrum of FAM-C<sub>6</sub>R. Dissolution method: 0.1 mg sample dissolved to 0.5 mL by 20% ACN and 80% H<sub>2</sub>O. Probe: ESI. Nebulizing gas flow: 1.5 L/min. CDL temperature: 250 °C. Block temperature: 200 °C. T. flow: 0.2 mL/min. B. conc: 50% H<sub>2</sub>O/50% MeOH. The results indicate the formation of FAM-C<sub>6</sub>R.

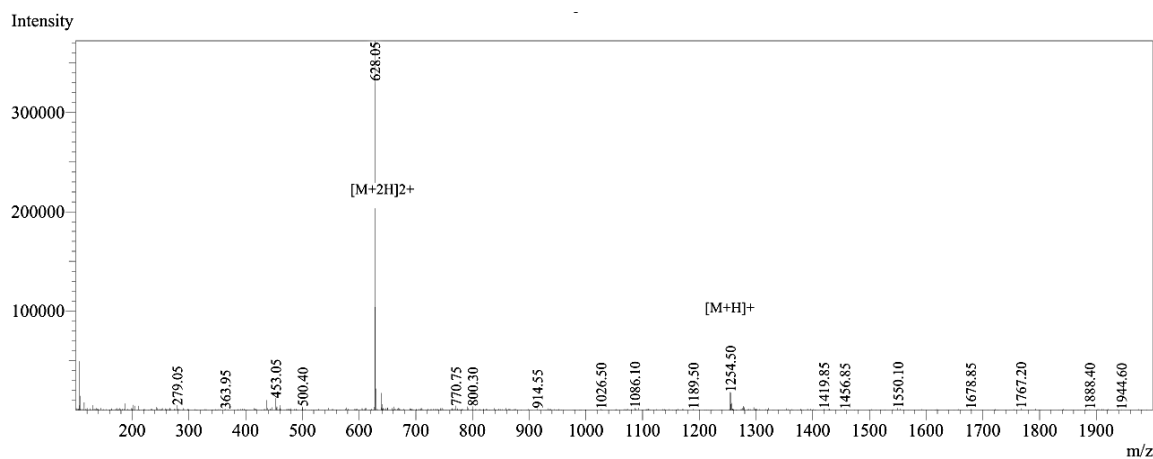


**Figure A5** Mass spectrum of FAM-C<sub>7</sub>R. Dissolution method: 0.1 mg sample dissolved to 0.5 mL by 25% ACN and 75% H<sub>2</sub>O. Probe: ESI. Nebulizing gas flow: 1.5 L/min. CDL temperature: 250 °C. Block temperature: 200 °C. T. flow: 0.2 mL/min. B. conc: 50% H<sub>2</sub>O/50% MeOH. The results indicate the formation of FAM-C<sub>7</sub>R.

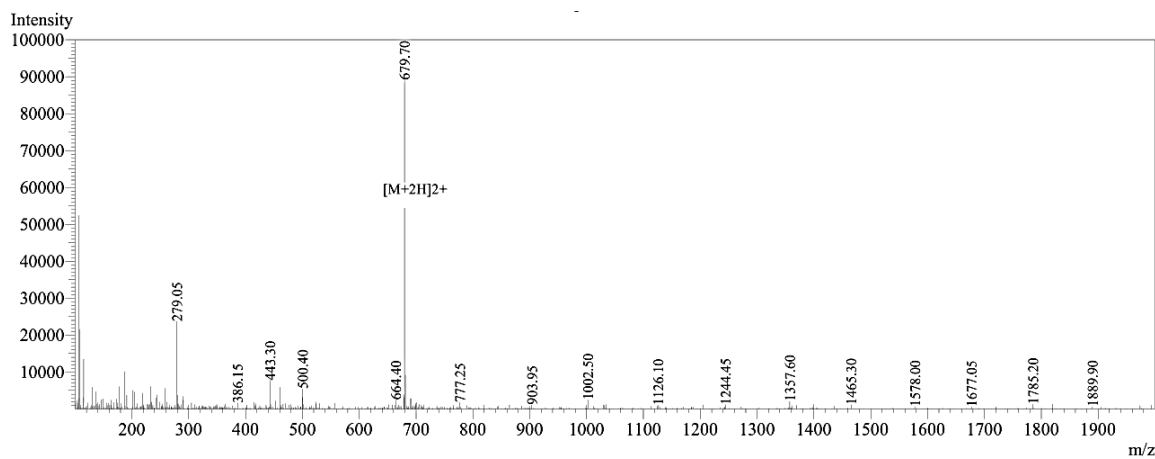


**Figure A6** Mass spectrum of FAM-C<sub>8</sub>R. Dissolution method: 0.1 mg sample dissolved to 0.5 mL by 25% ACN and 75% H<sub>2</sub>O. Probe: ESI. Nebulizing gas flow: 1.5 L/min. CDL temperature: 250 °C. Block temperature: 200 °C. T. flow: 0.2 mL/min. B. conc: 50% H<sub>2</sub>O/50% MeOH. The results indicate the formation of FAM-C<sub>8</sub>R.

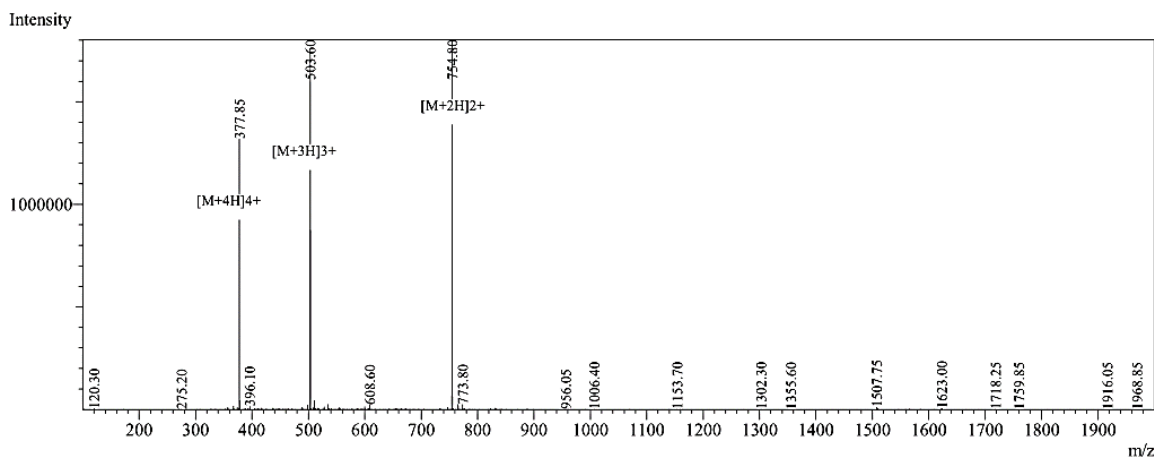


**Figure A7** Mass spectrum of Acetyl-RVRRF<sub>4</sub>KY. Dissolution method: 0.1 mg sample dissolved to 0.5 mL by 25% ACN and 75% H<sub>2</sub>O. Probe: ESI. Nebulizing gas flow: 1.5 L/min. CDL temperature: 250 °C. Block temperature: 200 °C. T. flow: 0.2 mL/min. B. conc: 50% H<sub>2</sub>O/50% MeOH.

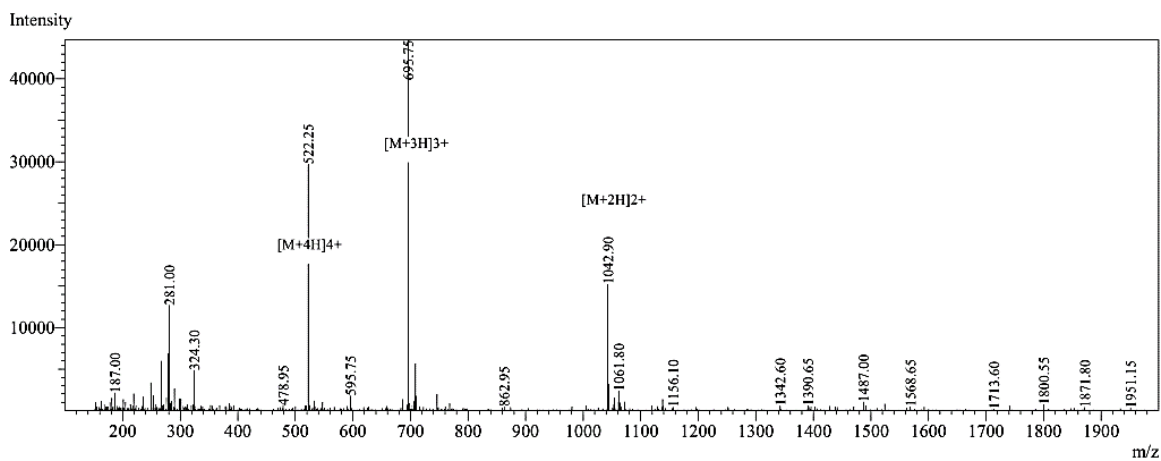


**Figure A8** Mass spectrum of C<sub>6</sub>RVRRF<sub>4</sub>KY. Dissolution method: 0.1 mg sample dissolved to 0.5 mL by 25% ACN and 75% H<sub>2</sub>O. Probe: ESI. Nebulizing gas flow: 1.5 L/min. CDL temperature: 250 °C. Block temperature: 200 °C. T. flow: 0.2 mL/min. B. conc: 50% H<sub>2</sub>O/50% MeOH.

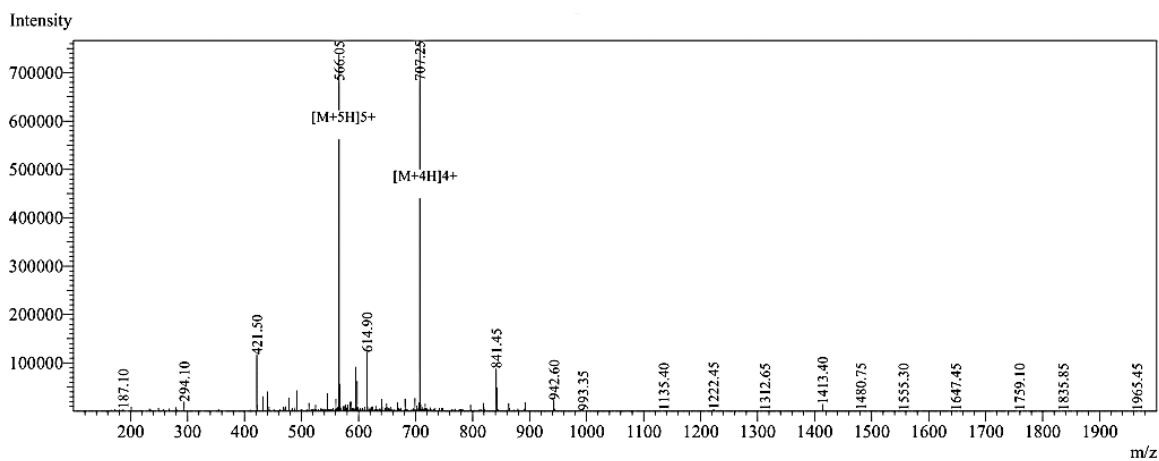


**Figure A9** Mass spectrum of C<sub>6</sub>K<sup>Dab</sup>RVRRK<sup>Dan</sup>F<sub>4</sub>KY (FRET labelled). Dissolution method: 0.1 mg sample dissolved to 0.5 mL by 25% ACN and 75% H<sub>2</sub>O. Probe: ESI. Nebulizing gas flow: 1.5 L/min. CDL temperature: 250 °C. Block temperature: 200 °C. T. flow: 0.2 mL/min. B. conc: 50% H<sub>2</sub>O/50% MeOH.



## SI References

- (1) Delaglio, F.; Grzesiek, S.; Vuister, G. W.; Zhu, G.; Pfeifer, J.; Bax, A., Nmrpipe: A Multidimensional Spectral Processing System Based on Unix Pipes. *J. Biomol. NMR* **1995**, *6*, 277-93.
- (2) Johnson, B. A.; Blevins, R. A., Nmr View: A Computer Program for the Visualization and Analysis of Nmr Data. *J. Biomol. NMR* **1994**, *4*, 603-614.
- (3) Maier, J. A.; Martinez, C.; Kasavajhala, K.; Wickstrom, L.; Hauser, K. E.; Simmerling, C., Ff14sb: Improving the Accuracy of Protein Side Chain and Backbone Parameters from Ff99sb. *J. Chem. Theory Comput.* **2015**, *11*, 3696-3713.
- (4) Maier, J. A.; Martinez, C.; Kasavajhala, K.; Wickstrom, L.; Hauser, K. E.; Simmerling, C., Case, D. A., Ben-Shalom, I. Y., Brozell, S. R., Cerutti, D. S., Cheatham, T. E., III, Cruzeiro, V. W. D., Darden, T. A., Duke, R. E., Ghoreishi, D., Gilson, M. K., Gohlke, H., Goetz, A. W., Greene, D., Harris, R., Homeyer, N., Izadi, S., Kovalenko, A., Kurtzman, T., Lee, T. S., Legrand, S., Li, P., Lin, C., Liu, J., Luchko, T., Luo, R., Mermelstein, D. J., Merz, K. M., Miao, Y., Monard, G., Nguyen, C., Nguyen, H., Omelyan, I., Onufriev, A., Pan, F., Qi, R., Roe, D. R., Roitberg, A., Sagui, C., Schott-Verdugo, S., Shen, J., Simmerling, C. L., Smith, J., Salomon-Ferrer, R., Swails, J., Walker, R. C., Wang, J., Wei, H., Wolf, R. M., Wu, X., Xiao, L., York, D. M., and Kollman, P. A. . *AMBER 2018*, University of California, San Francisco.
- (5) Wu, E. L.; Cheng, X.; Jo, S.; Rui, H.; Song, K. C.; Dávila-Contreras, E. M.; Qi, Y.; Lee, J.; Monje-Galvan, V.; Venable, R. M.; Klauda, J. B.; Im, W., Charmm-Gui Membrane Builder toward Realistic Biological Membrane Simulations. *J. Comput. Chem.* **2014**, *35*, 1997-2004.
- (6) Cheng, P. N.; Pham, J. D.; Nowick, J. S., The Supramolecular Chemistry of Beta-Sheets. *J. Am. Chem. Soc.* **2013**, *135*, 5477-5492.
- (7) An, H.-W.; Li, L.-L.; Wang, Y.; Wang, Z.; Hou, D.; Lin, Y.-X.; Qiao, S.-L.; Wang, M.-D.; Yang, C.; Cong, Y.; Ma, Y.; Zhao, X.-X.; Cai, Q.; Chen, W.-T.; Lu, C.-Q.; Xu, W.; Wang, H.; Zhao, Y., A Tumour-Selective Cascade Activatable Self-Detained System for Drug Delivery and Cancer Imaging. *Nat. Commun.* **2019**, *10*, 4861.
- (8) Cheng, D.-B.; Wang, D.; Gao, Y.-J.; Wang, L.; Qiao, Z.-Y.; Wang, H., Autocatalytic Morphology Transformation Platform for Targeted Drug Accumulation. *J. Am. Chem. Soc.* **2019**, *141*, 4406-4411.
- (9) Wang, M.; Wang, J.; Zhou, P.; Deng, J.; Zhao, Y.; Sun, Y.; Yang, W.; Wang, D.; Li, Z.; Hu, X.; King, S. M.; Rogers, S. E.; Cox, H.; Waigh, T. A.; Yang, J.; Lu, J. R.; Xu, H., Nanoribbons Self-Assembled from Short Peptides Demonstrate the Formation of Polar Zippers between B-Sheets. *Nat. Commun.* **2018**, *9*, 5118.
- (10) Feng, Z.; Wang, H.; Wang, S.; Zhang, Q.; Zhang, X.; Rodal, A. A.; Xu, B., Enzymatic Assemblies Disrupt the Membrane and Target Endoplasmic Reticulum for Selective Cancer Cell Death. *J. Am. Chem. Soc.* **2018**, *140*, 9566-9573.
- (11) Jentsch, T. J.; Hübner, C. A.; Fuhrmann, J. C., Ion Channels: Function Unravelling by Dysfunction. *Nat. Cell Biol.* **2004**, *6*, 1039-1047.
- (12) Agre, P., The Aquaporin Water Channels. *Proc. Am. Thorac. Soc.* **2006**, *3*, 5-13.
- (13) Li, R. S.; Gao, P. F.; Zhang, H. Z.; Zheng, L. L.; Li, C. M.; Wang, J.; Li, Y. F.; Liu, F.; Li, N.; Huang, C. Z., Chiral Nanoprobes for Targeting and Long-Term Imaging of the Golgi Apparatus. *Chem. Sci.* **2017**, *8*, 6829-6835.
- (14) Huang, C. Z.; Li, K. A.; Tong, S. Y., Determination of Nucleic Acids by a Resonance

Light-Scattering Technique with Alpha, Beta, Gamma, Delta-Tetrakis[4-(Trimethylammoniumyl)Phenyl]Porphine. *Anal. Chem.* **1996**, 68, 2259-2263.

(15) Pasternack, R. F.; Bustamante, C.; Collings, P. J.; Giannetto, A.; Gibbs, E. J., Porphyrin Assemblies on DNA as Studied by a Resonance Light-Scattering Technique. *J. Am. Chem. Soc.* **1993**, 115, 5393-5399.